The formation of disc galaxies in a ΛCDM universe

Oscar Agertz,[1][*] Romain Teyssier[1,2] and Ben Moore[1]

[1]*Institute for Theoretical Physics, University of Zürich, CH-8057 Zürich, Switzerland*
[2]*CEA Saclay, DSM/IRFU/SAp, Batiment 709, 91191 Gif-sur-Yvette Cedex, France*

ABSTRACT

We study the formation of disc galaxies in a fully cosmological framework using adaptive mesh refinement simulations. We perform an extensive parameter study of the main subgrid processes that control how gas is converted into stars and the coupled effect of supernovae feedback. We argue that previous attempts to form disc galaxies have been unsuccessful because of the universal adoption of strong feedback combined with high star formation efficiencies. Unless extreme amounts of energy are injected into the interstellar medium during supernovae events, these star formation parameters result in bulge-dominated S0/Sa galaxies as star formation is too efficient at $z \sim 3$. We show that a low efficiency of star formation more closely models the subparsec physical processes, especially at high redshift. We highlight the successful formation of extended disc galaxies with scalelengths $r_\mathrm{d} = 4$–5 kpc, flat rotation curves and bulge-to-disc ratios of $B/D \sim 1/4$. Not only do we resolve the formation of a Milky Way-like spiral galaxy, we also observe the secular evolution of the disc as it forms a pseudo-bulge. The disc properties agree well with observations and are compatible with the photometric and baryonic Tully–Fisher relations, the Σ_SFR–Σ_gas (Kennicutt–Schmidt) relation and the observed angular momentum content of spiral galaxies. We conclude that the underlying small-scale star formation physics plays a greater role than previously considered in simulations of galaxy formation.

Key words: methods: numerical – galaxies: evolution – galaxies: formation – galaxies: haloes – galaxies: spiral.

1 INTRODUCTION

The prevailing picture of galaxy formation emerged more than 30 yr ago (White & Rees 1978; Fall & Efstathiou 1980). Within the framework of the broadly accepted Λ cold dark matter (ΛCDM) scenario (Komatsu et al. 2009), gravity assembles structures in a bottom-up fashion. Haloes of dark matter acquire angular momentum via tidal torques (Peebles 1969; Fall & Efstathiou 1980) from interacting structures, and as gas cools and condenses into their central parts, star-forming galaxies form. A realistic angular momentum content can be accounted for if most of the angular momentum is retained in the assembly process. In this picture, the host halo is responsible for the final galaxy characteristics (e.g. Mo, Mao & White 1998). While several aspects of the theory of galaxy formation are still being developed, e.g. the underlying physics of the missing satellite problem (Klypin et al. 1999; Moore et al. 1999) and the role of cold stream accretion (Kereš et al. 2005, 2009; Dekel et al. 2009), the model has proven successful for understanding global properties of galaxy assembly.

Given the complexity and non-linearity of the involved processes, computer simulations have become the ideal tool for studying the formation of structure. The formation of a late-type spiral galaxy, such as our own Milky Way, has been studied numerically in fully ΛCDM cosmological context by many authors (e.g. Abadi et al. 2003b; Sommer-Larsen, Götz & Portinari 2003; Governato et al. 2004; Robertson et al. 2004; Okamoto et al. 2005; Governato et al. 2007; Agertz, Teyssier & Moore 2009; Croft et al. 2009; Piontek & Steinmetz 2009b; Scannapieco et al. 2009). To date, no attempt has yielded a realistic candidate. The dominant reason for this is the so-called 'angular momentum problem' which leads to small, centrally concentrated discs dominated by large bulges (Navarro & Benz 1991; Navarro & White 1994). Merging substructures lose angular momentum to the outer halo via dynamical friction, forcing the associated baryons to end up in the central parts of the protogalaxy as a spheroid rather than a disc. This poses a problem for the theoretical understanding of extended late-type galaxies. This might in part stem from numerical issues: the commonly used smoothed particle hydrodynamics (SPH) (Gingold & Monaghan 1977; Lucy 1977) technique is known to incorrectly treat boundaries, hence poorly treating multiphase fluids (e.g. Agertz et al. 2007; Read, Hayfield & Agertz 2010). This can lead to artificial angular momentum transfer at the interface between a cold disc and a hot halo (Okamoto et al. 2005).

A number of proposed solutions to the angular momentum problem exist, all amounting to the same process: keep the gas from

[*]E-mail: agertz@physik.uzh.ch

cooling and forming stars too efficiently in the merging dark matter satellites at high redshift. One natural source is the cosmological UV background, being responsible for reionization at $z \gtrsim 6$ which heats the gas, preventing it to cool efficiently into star-forming dwarf galaxies (Thoul & Weinberg 1996; Quinn, Katz & Efstathiou 1996; Gnedin 2000; Hoeft et al. 2006). However, the impact on objects larger than $v_{circ} \sim 10\,\mathrm{km\,s^{-1}}$ is unclear due to e.g. self-shielding and efficient collisional cooling (Dijkstra et al. 2004).

Gas in low-mass haloes can also be blown out by supernova-driven winds (Dekel & Silk 1986; Efstathiou 2000), hence lowering the resulting star formation efficiency (SFE), enriching the intergalactic medium (IGM) in the process. Mac Low & Ferrara (1999) demonstrated that while dwarf galaxies of mass 10^6–$10^9\,\mathrm{M_\odot}$ efficiently can expel metals in supernovae-driven winds, virtually no mass is lost for systems of mass $\gtrsim 10^7\,\mathrm{M_\odot}$ (see also Dubois & Teyssier 2008). The inefficiency in driving winds from dwarfs was also reported by Marcolini et al. (2006) who attributed this to the extended dark matter halo and efficient metal cooling. In this scenario, mass-loss and IGM enrichment will occur due to tidal and ram-pressure stripping (e.g. Mori & Burkert 2000). Phenomenological models of e.g. momentum-driven winds have proven successful in reproducing the high-z IGM (Oppenheimer & Davé 2006) but it is uncertain how it regulates star formation and in what manner the expelled gas is re-accreted at later times (Oppenheimer et al. 2010).

Various recipes of supernovae feedback have been developed for numerical simulations (e.g. Navarro & White 1993; Kay et al. 2002; Scannapieco et al. 2006), and the methods have proven successful in removing low-angular-momentum material from the central parts of galaxies (e.g. Sommer-Larsen et al. 2003; Okamoto et al. 2005; Governato et al. 2007), yielding more extended galaxies in comparison to models without feedback. However, it is unclear as to what extent this way of reducing star formation can account for disc-dominated spiral galaxies like the Milky Way. Recently Scannapieco et al. (2009) demonstrated numerically, in a fully cosmological setting, how a set of eight Milky Way-sized haloes failed to form significant discs. While half of the sample were early-type galaxies resulting from late time mergers, the other half of the sample had less than 20 per cent of their stellar mass in discs. This can be a result of the inability of the adopted feedback to remove or redistribute low-angular-momentum material, but is also a strong indication that something else might regulate star formation at high redshift. On the same topic, Sawala et al. (2010) argues that modern simulations of dwarf galaxy formation (Valcke, de Rijcke & Dejonghe 2008; Stinson et al. 2009; Governato et al. 2010) all yield much larger stellar masses than expected from observations as well as gas-to-star conversion efficiencies almost an order of magnitude too large. Dutton & van den Bosch (2009) found that, for SNe feedback to yield realistic galaxies, it must be very efficient, converting 25 per cent of the SN energy into outflows. If too strong a feedback is employed, the discs can be destroyed by internal processes as too much material is ejected into the halo, preventing efficient disc reformation from cold gas, and possibly violating the upper bounds of halo gas found in X-ray surveys [see Bregman (2007) and references within]. In light of these studies, it is unclear if supernovae feedback is the sole agent in regulating star formation. Note that SNe explosions can regulate star formation in galaxies without expelling gas, being a driver of galactic turbulence (Mac Low & Klessen 2004).

Fundamentally, star formation is regulated by the availability of H_2. The observed Kennicutt-Schmidt (from now on K–S) relation (Kennicutt 1998), that relates Σ_{SFR} to Σ_{gas}, varies strongly among individual spiral galaxies and cannot be fitted with a single power law (Bigiel et al. 2008). Σ_{SFR} behaves very differently for Σ_{gas} greater or smaller than $\approx 9\,\mathrm{M_\odot\,pc^{-2}}$, marking the transition from atomic to fully molecular star-forming gas (Leroy et al. 2008), and is dependent on gas metallicity, dust content, turbulence, small-scale clumpiness and local dissociating UV field (McKee & Ostriker 2007). The inclusion of these processes and its impact on global star formation in discs has recently been studied both numerically (Robertson & Kravtsov 2008; Gnedin, Tassis & Kravtsov 2009; Pelupessy & Papadopoulos 2009) as well as analytically (e.g. Krumholz, McKee & Tumlinson 2009). A natural outcome of this treatment is an order of magnitude lower amplitude of the K–S relation at high redshifts ($z \sim 3$) (Gnedin & Kravtsov 2010b). This agrees well with the observation of damped Lyα systems (DLA: Wolfe & Chen 2006) as well as Lyman Break Galaxies (Rafelski et al. 2009). This indicates that star formation can be made inefficient at high redshift, leaving gas for late-time star formation in a disc like environment, but not necessarily by expelling gas in supernova-driven winds. In addition, Murray, Quataert & Thompson (2010) argue that the disruption time-scale of giant molecular clouds (GMCs) due to jets, H II gas pressure, and radiation pressure also serves to regulate the SFE in galaxies. The disruption occurs well before the most massive stars exit the main sequence, meaning that supernovae in principle have little effect on GMC lifetimes.

In this paper we investigate to what extent supernovae feedback and the underlying small-scale star-forming physics can affect the formation and evolution of realistic spiral galaxies in a fully cosmological setting. The former effect is studied via well-tested numerical implementations of SNII, SNIa feedback coupled to metal enrichment, as well as stellar mass-loss. The latter influence is achieved by considering different normalizations of the Schmidt-law star formation efficiency. We conduct a comprehensive analysis of the resulting $z = 0$ discs and compare them to observational relations.

The paper is organized as follows. In Section 2, we describe the numerical method used in this work, including the adopted feedback and star formation prescriptions. In Section 3, we present the cosmological initial conditions and discuss the free parameters of this work. Section 4 outlines the disc analysis and summarizes the final properties of the simulation suite. In Sections 5 and 6, we present a detailed analysis of the impact of small-scale SFE and supernova feedback, respectively. In Section 7 we compare our simulations to modern observations. Finally, Section 8 summarizes and discusses our conclusions.

2 NUMERICAL FRAMEWORK

We use the adaptive mesh refinement (AMR) code RAMSES (Teyssier 2002) to simulate the formation of a massive disc galaxy in a cosmological context including dark matter, gas and stars. The gas dynamics is calculated using a second-order unsplit Godunov method, while collisionless particles (including stars) are evolved using the particle-mesh technique. The equation of state of the gas is that of a perfect mono-atomic gas with an adiabatic index $\gamma = 5/3$. Self-gravity of the gas is calculated by solving the Poisson equation using the multigrid method (Brandt 1977) on the coarse grid and by the conjugate gradient method on finer ones. The modelling includes realistic recipes for star formation (Rasera & Teyssier 2006), supernova feedback and enrichment (Dubois & Teyssier 2008). Details on these implementations are given below. Metals are advected as a passive scalar and are incorporated self-consistently in the

cooling and heating routine. The code adopts the cooling function of Sutherland & Dopita (1993) for cooling at temperatures 10^4–$10^{8.5}$ K. We extend cooling down to 300 K using rates from Rosen & Bregman (1995). Gas metallicity is also accounted for in the cooling routines. A UV background is considered using the prescription of Haardt & Madau (1996). In order to model a subgrid gaseous equation of state, hence avoiding artificial gas fragmentation, the gas is given a polytropic equation of state,

$$T = T_0 \left(\frac{\rho}{\rho_0} \right)^{\gamma_0 - 1}, \tag{1}$$

for densities large than ρ_0. Throughout this paper we adopt $T_0 = 1000$ K and $\gamma_0 = 2.0$. In this work, the polytrope density is set equal to the star formation threshold n_0. Following Agertz et al. (2009), we adopt an initial metallicity of $Z = 10^{-4}\, Z_\odot$ in the high-resolution region. This also serves as a flag for allowed regions of refinement. The refinement strategy is based on a quasi-Lagrangian approach, so that the number of particles per cell remains roughly constant, avoiding discreteness effects (e.g. Romeo et al. 2008).

2.1 Star formation

To model the conversion of gas into stars, we adopt a Schmidt law (Schmidt 1959) of the form

$$\dot{\rho}_g = -\epsilon_{ff} \frac{\rho_g}{t_{ff}} \quad \text{for } \rho > \rho_0, \tag{2}$$

where ρ_g is the gas density, $t_{ff} = \sqrt{3\pi/32G\rho}$ is the local free-fall time, ϵ_{ff} is the star formation efficiency per free-fall time and ρ_0 is the threshold for star formation. As soon as a cell is eligible for star formation, particles are spawned using a Poisson process where the stellar mass, m_*, is chosen to be a multiple of $\rho_0 \Delta x^3$. Each formed star particle is treated as one stellar population with an associated initial mass function (IMF). This is a relevant approximation as the star particle masses are orders of magnitude larger than the average stellar masses. We also ensure that no more than 90 per cent of the gas in a cell is depleted by the star formation process.

The ρ_0 and ϵ_{ff} parameters in equation (2) are, in addition to being unconstrained physical parameters, resolution and hence scale dependent. There are in a sense two regimes of star formation in global simulations of disc galaxies as follows.

(i) The ISM is resolved: At parsec-scale resolution, star formation occurs in their natural sites i.e. massive clouds such as GMCs. Modern estimates of star formation efficiencies by Krumholz & Tan (2007) point towards values of $\epsilon_{ff} = 1$–2 per cent at densities of $n \sim 10^2$–10^5 cm^{-3}. To only allow for star formation to take place in the actual physical star formation sites, hence tracing the formation of H_2, allows for more accurate predictions of e.g. the Kennicutt–Schmidt star formation relation with less of a requirement to tune numerical parameters (see e.g. Gnedin et al. 2009). This treatment leads to $\rho_g \rightarrow \rho_{H_2}$ in equation (2), which is equivalent to ϵ_{ff} being dependent on the environment, due in part to the local H_2 fraction. On galactic scales, this means that the scaleheight of all ISM components are resolved using at least 10 resolution elements (Romeo 1994). If this is not satisfied, the true disc stability will not be modelled accurately. This treatment is the goal of most simulations, but is due to the computational load beyond the capabilities of modern simulations attempting to study the assembly and evolution of large spiral galaxies to $z = 0$. Isolated simulations of large spiral galaxies in a non-cosmological setting have successfully reached this resolution (Agertz et al. 2009; Tasker & Tan 2009), albeit with simplified physics. As the star formation sites become resolved, new physics

becomes important e.g. radiative feedback in order to accurately treat the lifetimes of GMC structures (Murray et al. 2010).

(ii) The ISM is under-resolved: To radially resolve a Milky Way like galactic disc, i.e. sampling the scale radius with at least 10 resolution elements, a force and hydro resolution of a few 100 pc is necessary. At this resolution the scaleheight is captured with more or less one resolution element. The true disc stability can be affected as both the density and velocity structure (gas and stellar dispersion) are influenced numerically. This still allows for the disc to have the correct global properties such as gas and stellar mass compositions, thin and thick disc, and even to develop realistic spiral structure. In this case a statistical star formation recipe based on the local gas density and free-fall time is well motivated both theoretically and observationally.

As we will describe in Section 3.1, we are targeting the latter regime of subgrid star formation and will investigate some of the numerical caveats related to it. At resolutions of several 100 pc, the ϵ_{ff} parameter absorbs the small-scale physics regulating star formation, allowing for a qualitative influence on galaxy formation. We note that there are alternative formulation of gas-to-star conversion laws in the literature [see e.g. Leroy et al. (2008) for a comprehensive summary]. However, as they are all designed to fit an observed relation, and all include a normalization constant similar to ϵ_{ff}, we believe equation (2) is a representative choice for this study.

2.2 Supernovae and stellar feedback

The standard recipe for supernova feedback in RAMSES involves only Type II supernovae events (SNII). We have also implemented additional treatment of Type Ia events (SNIa) as well as mass-loss via stellar winds. Including all of these effects is important as a single stellar population can return up to 30–40 per cent of its mass to the ISM during its lifetime. The implementations are as follows.

2.2.1 Type II

Type II SN events are relevant for stellar masses of 8–40 M$_\odot$ which represents $\sim$10 per cent of the mass of a stellar population, regardless of IMF. We assume that 10 Myr after a star particle is formed, 10 per cent of the star particle's mass is injected into the nearest gas cell together with a total energy of $E_{SNII} = 10^{51}\,(m_{ejecta}/10\,\mathrm{M_\odot})$ erg in thermal energy. At low resolution, this energy would quickly radiate away (Katz 1992) in the dense gas, without allowing for an adiabatic expansion of the supernova blast-wave (McKee & Ostriker 1977). To remedy this, we turn off cooling in cells containing young stars to allow for the blast-wave to grow and be resolved by few cells, hence converting thermal energy into PdV work (see e.g. Gerritsen 1997). In detail, for every star formation event, the inverse of the birth time, $1/t_{bt}$, is stored in the computational grid, overwriting any previous value. This passive scalar field is advected with the hydro flow (the conserved quantity is ρ_{gas}/t_{bt}). Gas cooling at a simulation time t_{sim} is only allowed if $t_{sim} - t_{bt} > \Delta t_{off}$, where Δt_{off} is the cooling shut-off time-scale. Calculations of relevant time-scales and numerical tests using the SPH formalism was carried out by Stinson et al. (2006). Relevant time-scales are on the order of tens of Myr and we adopt $\Delta t_{off} = 50$ Myr.

2.2.2 Type Ia

We treat SNIa and stellar mass-loss using the prescription outlined in Raiteri, Villata & Navarro (1996). The assumed IMF is the

parametrization by Kroupa, Tout & Gilmore (1993), which for a star particle of mass m_* reads

$$\Phi(M) = m_* A \begin{cases} 2^{0.9} M^{-1.3} & \text{for } 0.08 \leq M < 0.5\,\mathrm{M_\odot} \\ M^{-2.2} & \text{for } 0.5 \leq M < 1\,\mathrm{M_\odot} \\ M^{-2.7} & \text{for } M \geq 1\,\mathrm{M_\odot}, \end{cases}$$

where M is the stellar mass in units of $\mathrm{M_\odot}$ and the normalization constant $A \approx 0.3029$. The adopted lower and upper limits are $0.08\,\mathrm{M_\odot}$ and $100\,\mathrm{M_\odot}$, respectively. At each simulation time-step, we calculate the mass fraction of each star particle ending its H and He burning phase, i.e. leaving the main sequence, using the fit

$$\log t_* = a_0(Z) + a_1(Z)\log M + a_2(Z)(\log M)^2, \tag{3}$$

where t_* is the lifetime of the star and Z the metallicity. The adopted coefficients and references to the original data can be found in Raiteri et al. (1996). Progenitors of SNIa are carbon plus oxygen white dwarfs that accrete mass from binary companions. Stellar evolution theory predict the binary masses to be in the range of ~ 3–$16\,\mathrm{M_\odot}$. The number of SNIa events within a star particle, at a given simulation time with an associated time-step Δt, is

$$N_{\mathrm{SNIa}} = \int_{m_t}^{m_{t+\Delta t}} \hat{\Phi}(M_2)\,\mathrm{d}M_2, \tag{4}$$

where m_t and $m_{t+\Delta t}$ is the mass interval of stars ending their life during the computational time-step. $\hat{\Phi}(M_2)$ is the IMF of the secondary star, i.e.

$$\hat{\Phi}(M_2) = m_* A' \int_{M_{\mathrm{inf}}}^{M_{\mathrm{sup}}} \left(\frac{M_2}{M_B}\right)^2 M_B^{-2.7}\,\mathrm{d}M_B, \tag{5}$$

where M_B is the mass of the binary, $M_{\mathrm{inf}} = \max(2M_2,\,3\,\mathrm{M_\odot})$ and $M_{\mathrm{sup}} = M_2 + 8\,\mathrm{M_\odot}$. The constant $A' = 0.16A$, and is a calibrated value for SNIa events in our Galaxy (van den Bergh & McClure 1994). Each explosion is assumed to release 10^{51} erg (released as thermal energy in the nearest gas cell) and $0.76\,\mathrm{M_\odot}$ of metal-enriched material ($0.13\,\mathrm{M_\odot}$ of $^{16}\mathrm{O}$ and $0.63\,\mathrm{M_\odot}$ of $^{56}\mathrm{Fe}$) (Thielemann, Nomoto & Yokoi 1986).

2.2.3 Stellar mass-loss

For each time-step Δt, and star particle, we calculate the average stellar mass, $\langle M \rangle$, exiting the main sequence using equation (3). The mass-loss during the Δt time-span is calculated using the best-fitting initial–final mass relation of Kalirai et al. (2008):

$$M_{\mathrm{wind}} = 0.891 - 0.394/\langle M \rangle. \tag{6}$$

At each time interval Δt, the total mass-loss in winds is

$$M_{\mathrm{tot,wind}} = f_m m_* M_{\mathrm{wind}}, \tag{7}$$

where

$$f_m = \int_{m_t}^{m_{t+\Delta t}} \Phi(M)\,\mathrm{d}M. \tag{8}$$

The lost stellar mass enters the gaseous mass in the nearest cell and the gas metallicity is updated consistently with the star particle's metallicity.

3 INITIAL CONDITIONS AND SIMULATION SUITE

The initial conditions used in this work are a subset the Silver River simulation suite (Potter et al. in preparation), aimed to study the pure dark matter assembly history of a Milky Ways size halo in much greater detail than here. We adopt a *WMAP5* (Komatsu et al. 2009) compatible cosmology, i.e. a ΛCDM Universe with $\Omega_\Lambda = 0.73$, $\Omega_{\mathrm{m}} = 0.27$, $\Omega_{\mathrm{b}} = 0.045$, $\sigma_8 = 0.8$ and $H_0 = 70\,\mathrm{km\,s^{-1}\,Mpc^{-1}}$.

The upcoming work by Potter et al. will present the details concerning the initial condition generation. Briefly, a pure dark matter simulation was performed using a simulation cube of size $L_{\mathrm{box}} = 179$ Mpc. At $z = 0$, a halo of mass $M_{200,\mathrm{c}} \approx 9.7 \times 10^{11}\,\mathrm{M_\odot}$ was selected for resimulation at high resolution, and traced back to the initial conditions at $z = 133$. $M_{200,\mathrm{c}}$ is the virial mass of the halo, defined as the mass enclosed in a sphere with mean density 200 times the critical value. The corresponding virial radius is $r_{200,\mathrm{c}} = 205$ kpc. By using a definition based on 200 times the background density, we obtain $M_{200,\mathrm{bg}} = 1.25 \times 10^{12}\,\mathrm{M_\odot}$ and $r_{200,\mathrm{bg}} = 340$ kpc. When baryons are included in the simulations, the final *total* halo mass remains roughly the same.

The halo has a quiet merger history, i.e. it undergoes no major merger after $z = 1$, which favours the formation of a late-type galaxy. A nested hierarchy of initial conditions for the dark matter and baryons was generated using the GRAFIC++[1] code, where we allow for the high-resolution particles to extended to three virial radii from the centre of the halo at $z = 0$. This avoids mixing of different mass dark matter particles in the inner parts of the domain. In this work, we focus on two sets of resolutions from the Silver River suite, referred to as SR5 and SR6. The simulations are identical apart from the number of dark matter particles, and hence particle mass, as well as maximal AMR refinement. In SR6 the dark matter particle mass is $m_{\mathrm{DM}} = 2.5 \times 10^6\,\mathrm{M_\odot}$ and in SR5 $m_{\mathrm{DM}} = 3.2 \times 10^5\,\mathrm{M_\odot}$. The mesh is refined if a cell contains more than eight dark matter particles, and a similar criterion is employed for the baryonic component. At the maximum level of refinement, the simulations reach a physical resolution of $\Delta x = 170$ pc and $\Delta x = 340$ pc in SR5 and SR6, respectively.

3.1 The free parameters

The goal of this work is to study how the characteristics of disc galaxies change when standard numerical parameters governing star formation are modified. Following the discussion in Section 1, we consider star formation regulation in two different ways: small-scale (~ 100 pc) physics such as H_2 abundance, GMC turbulence, metallicity, radiative effects etc., or via energy injection from supernovae explosions leading to gas expulsion in galactic winds. The first mechanism is modelled by varying the Schmidt law (equation 2) SFE, ϵ_{ff}, which acts on a cell-by-cell basis. The latter is studied by increasing the injected SNII energy, E_{SNII}. In addition we study the impact of star formation threshold n_0, but in lesser detail.

The traditional way of treating star formation in simulations of galaxy formation (e.g. Governato et al. 2007; Piontek & Steinmetz 2009b) is to tune the SFE parameter using an isolated disc model to match the observed K–S relation, most commonly the fitting formula given by Kennicutt (1998) of $z = 0$ galaxies. In addition, the recipe for energy injection via supernovae and its efficiency is tuned simultaneously. These parameters are then used in fully cosmological simulation of galaxy formation. This scheme assumes that supernova explosions are the main sources of star formation regulation at high redshift. As argued in Section 1, the numerically assumed constant efficiency is strongly redshift dependent and a $z = 0$ tuning is likely to overpredict star formation in more metal

---

[1] http://grafic.sourceforge.net/

poor environment at higher redshifts. We treat ϵ_{ff} as a free, but constant, parameter and adopt $\epsilon_{\mathrm{ff}} = 1$, 2 or 5 per cent in the fully cosmological context. These values are in agreement with GMC estimates from Krumholz & Tan (2007). As we will demonstrate below, values lower than what is traditionally adopted is preferred in order to form late-type galaxies. Note that $\epsilon_{\mathrm{ff}} \approx 2c_*$, where c_* is the efficiency parameter used in e.g. Governato et al. (2007) and Scannapieco et al. (2009) (defined via $t_{\mathrm{dyn}} = 1/\sqrt{4\pi G\rho}$). Values of $c_* = 0.05$–0.1 are commonly employed i.e. a few times, up to an order of magnitude larger than what we consider here.

The standard SNII feedback described in Section 2.2.1 is the baseline feedback in all of our simulations. In a subset of simulations we add the additional stellar mass-loss and SNIa treatment. The high-efficiency simulation ($\epsilon_{\mathrm{ff}} = 5$ per cent) is used as a template for the impact on the injected feedback SNII energy, which we set to $E_{\mathrm{SNII}} = 1$, 2 and 5×10^{51} erg. Using energies that are several times larger than the canonical 10^{51} erg might be perceived as unrealistic, but we believe it is illustrative to study the extreme cases of this type of feedback. In addition, the amount of SNII energy dissipated in cooling, after the shut-off time has passed, is complicated to measure. As a control set we also run the simulations without feedback, both with and without metal enrichment.

The philosophy of the star formation threshold is as follows. In reality stars form in molecular clouds of average densities of $n > 10^2$ cm^{-3}. Imposing a threshold of this magnitude would require a resolution on the order of parsecs to resolve the formation of the star-forming clouds, something that is beyond the scope of fully cosmological hydro+N-body simulations today (but see Gnedin et al. 2009). We adopt $n_0 = 0.1$ and 1 cm^{-3} for each setting of ϵ_{ff}, but the appropriate choice is fundamentally tied to resolution and can lead to spurious results. The ISM has been shown to be represented by a lognormal density probability distribution function (PDF) (e.g. Kravtsov 2003; Wada & Norman 2007), or even a superposition of several lognormally distributed ISM phases (Robertson & Kravtsov 2008). The amount of gas eligible for star formation is represented by the high density part of the PDF which in turn is a

function of total disc gas mass and turbulence. A density threshold should be picked to allow for the high-density star-forming part of the PDF to be well resolved or at least contains, given an adopted numerical resolution, a converged amount of star-forming mass. If not, then chosen threshold will affect the numerical efficiency for global star formation. We will demonstrate this effect below.

In summary, the varied constants of interest here are the star formation threshold (n_0), the star formation efficiency per free-fall time (ϵ_{ff}) and the form of supernova feedback and injected energy (E_{SNII}). Our main focus is the impact of these parameters at the SR6 level of resolution, and we present a brief resolution study in Appendix A. We summarize our complete test suite in Table 1.

4 THE DISCS

In this work, we focus primarily on the disc properties in the SR6 simulations at $z = 0$. Details of the satellite galaxies and halo properties will be considered in a future work. Figs 1 and 2 show projected face-on and edge-on stellar and gas density maps at $z = 0$ for the galaxies in the star formation efficiency and feedback test suite, respectively. The discs show a wide range of spiral galaxy morphologies, and will return to this point in Section 5.4. We decompose the resulting stellar discs into a bulge, bar and disc component and fit these simultaneously into the stellar surface density profile. The latter is calculated using all stars out to a height of $|z| = 2.5$ kpc. For the bulge and disc component we assume exponential profiles, i.e.

$$\Sigma(r) = \Sigma_0 \exp(-r/r_{\mathrm{d}}), \tag{9}$$

where we fit for Σ_0 and the scale radius r_{d}. The bar component is modelled using a simple Gaussian,

$$\Sigma_{\mathrm{bar}}(r) = \frac{A_0}{\sigma} \exp\left[-\frac{(r - r_0)^2}{2\sigma^2}\right], \tag{10}$$

where we fit for the width σ, the central point r_0 and amplitude A_0. We consider this a conservative estimate of the bar mass as

Table 1. Summary of the numerical parameters. The simulations use a maximum physical cell resolution of $\Delta x = 340$ pc (SR6) or $\Delta x = 170$ pc (SR5), and the high-resolution region is occupied by dark matter particles of mass $m_{\mathrm{DM}} = 2.5 \times 10^6$ M$_\odot$ (SR6) or $m_{\mathrm{DM}} = 3.25 \times 10^5$ M$_\odot$ (SR5). All simulations use delayed cooling in regions of young stars, unless specified. When SNII feedback is used $E_{\mathrm{SNII}} = 10^{51}$ erg, unless other values are indicated.

| Run	ϵ_{ff} (per cent)	Feedback	Star formation threshold, n_0 (cm^{-3})
SR6-n01e1	1	SNII	0.1
SR6-n01e2	2	SNII	0.1
SR6-n01e5	5	SNII	0.1
SR6-n01e1ML	1	SNII, SNIa, mass-loss	0.1
SR6-n01e2ML	2	SNII, SNIa, mass-loss	0.1
SR6-n01e5ML	5	SNII, SNIa, mass-loss	0.1
SR6-n1e1	1	SNII	1
SR6-n1e2	2	SNII	1
SR6-n1e5	5	SNII	1
SR6-n1e1ML	1	SNII, SNIa, mass-loss	1
SR6-n1e2ML	2	SNII, SNIa, mass-loss	1
SR6-n01e1NFB	1	No feedback, $E_{\mathrm{SNII}} = 0$	0.1
SR6-n01e5NFB	5	No feedback, $E_{\mathrm{SNII}} = 0$	0.1
SR6-n01e5NFBmet	1	No feedback but metal enrichment	0.1
SR6-n01e5SN2	5	SNII, $E_{\mathrm{SNII}} = 2 \times 10^{51}$ erg	0.1
SR6-n01e5SN5	5	SNII, $E_{\mathrm{SNII}} = 5 \times 10^{51}$ erg	0.1
SR5-n1e1ML	1	SNII, SNIa, mass-loss	1
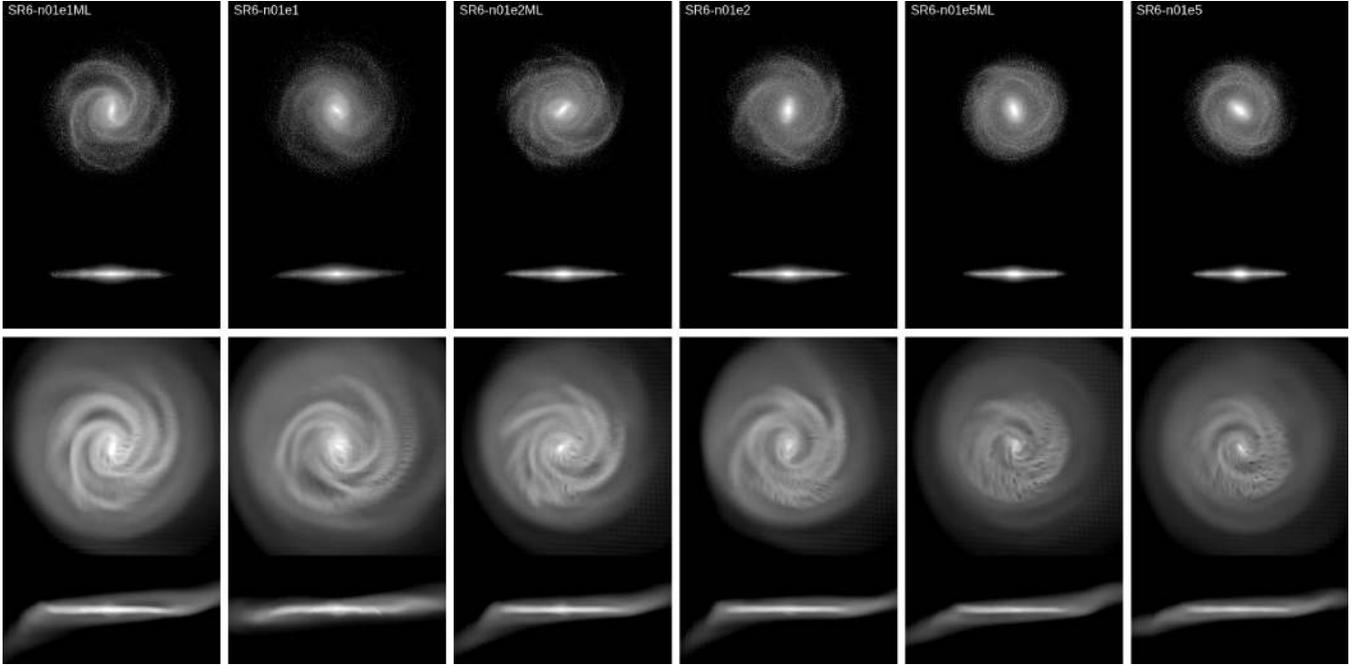
Figure 1. Projected face-on and edge-on surface density maps of the stars (top) and gas (bottom) of the $z = 0$ discs, where each panel is 60 kpc across. As the SFE is lowered and mass-loss is employed, spiral structure becomes more pronounced due to a less massive bulge. The Hubble type of the disc changes from an early-type (S0 or Sa) disc, to a late-type spiral galaxy (Sb or Sbc) as we decrease $\epsilon_{\rm ff}$.
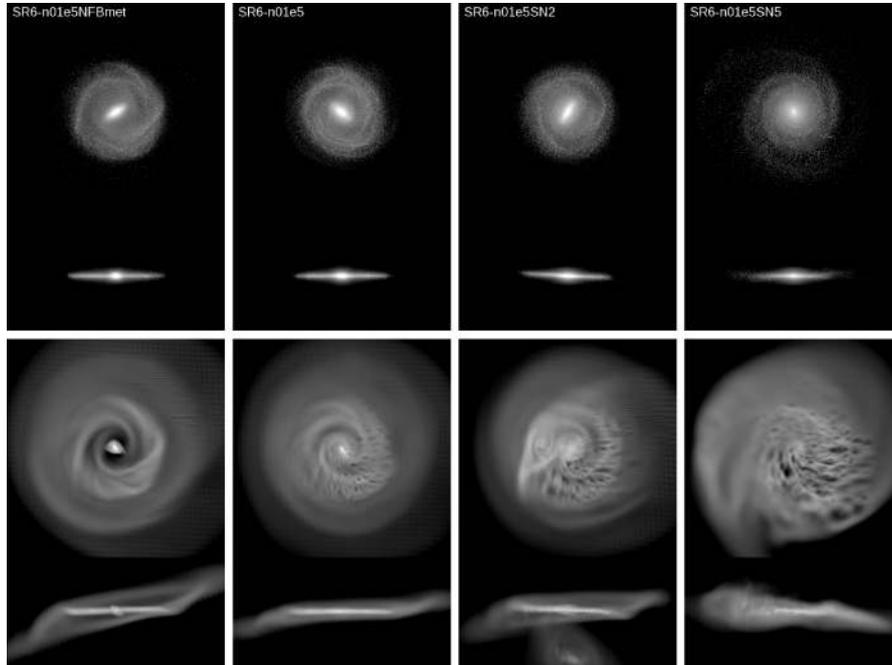
Figure 2. Projected face-on and edge-on surface density maps of the stars (top) and gas (bottom) of the $z = 0$ discs where each panel is 60 kpc across. From left to right, the feedback strength is $E_{\rm SNII} = 0, 1, 2$ and 5×10^{51} erg. As the injected amount of energy is increased, the gas component becomes more distorted.

a Gaussian contribution falls off towards the centre of the disc, leaving more mass to be accounted for by the bulge. An example of the fitting procedure can be seen in Fig. 3. The necessity of a separate bar component is clearly illustrated here. In the more bulge-dominated cases the bar amplitude is decreased considerably, owing to the weaker disc self-gravity.

The bulge mass, $M_{\rm bulge} = 2\pi\Sigma_{\rm bulge}r_{\rm bulge}^2$, is obtained by integrating equation (9). A similar relation holds for the disc, where we

also include the stellar disc mass past the break radius in the quoted disc stellar mass, $M_{\rm disc,s}$, but we only use the data within the break when fitting (see Fig. 3). The bar mass is simply the integrated mass from equation (10), and we consider the bar as a part of the disc component and include it in the quoted $M_{\rm disc,s}$. Doing this or not modifies the disc mass only slightly, especially in bulge-dominated galaxies. The gas is treated as a single component, and we simply consider the mass within $r = 15$ kpc and $|z| = 2.5$ kpc as the gaseous
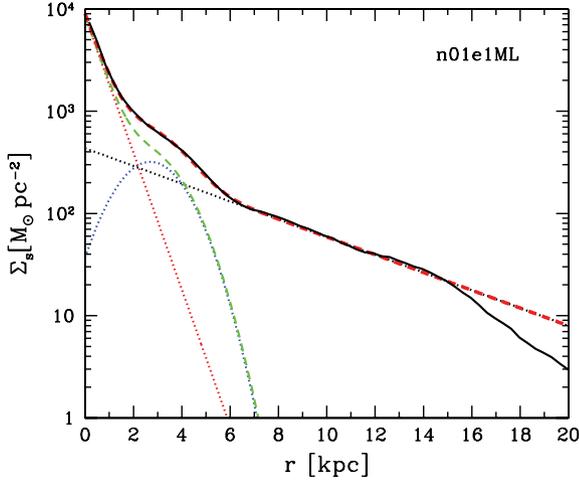
Figure 3. Example of a multicomponent fit (red dashed line) to the stellar surface density (black solid line) of the $z = 0$ disc in n01e1ML. The fit is composed of a bulge (red dotted line), a bar (blue dotted line) and a disc (black dotted line) component. The green dashed line shows the bulge and bar surface density contribution.

disc mass, $M_{disc,g}$. We consider only the stars when calculating the bulge-to-disc (B/D) and bulge-to-total (B/T) ratios. All measured and derived quantities are summarized in Table 2. We note that this method of defining galactic components in simulations, as well as others e.g. via angular momentum (Okamoto et al. 2005; Scannapieco et al. 2009), carry uncertainties.

Our simulated discs span a large range of characteristics: stellar disc masses are in the range $M_{disc,s} = 5$–$9 \times 10^{10}\,M_\odot$, bulge masses of $M_{bulge,s} = 2$–$7\,M_\odot$, B/D $\sim$0.23–1.2 and gas fractions $f_g = 0.05$–0.28. The scale radii of the discs, r_d, vary from typically 4–5 kpc to $>$10 kpc in the bulge-dominated systems. As we demonstrate below, extended disc galaxies of Sb, or even Sbc type, form only when star formation is numerically resolved in the

whole disc ($n_0 = 0.1\,\mathrm{cm}^{-3}$), and a low-efficiency $\epsilon_{ff} \sim 1$ per cent (or *very* strong feedback) is adopted. At larger efficiencies we observe how the B/D ratios increase, the discs are less extended, the rotational velocities peak at very large values and the spiral patterns become more tightly wound and less pronounced. This indicates a shift towards early-type discs like Sa or even S0.

5 EFFECT OF STAR FORMATION PARAMETERS

In this section we study the influence of star formation parameters, i.e. in essence the small-scale physics, on disc properties at $z = 0$. The resulting stellar surface densities (Σ_s), gas surface densities (Σ_{gas}) and rotational velocities measured from the gas (v_{rot}) are presented in Figs 4 and 5 for the first 11 simulations in the SR6 suite at $z = 0$ (see Table 1).

5.1 The star formation density threshold, n_0

We start by focusing on the data presented in Fig. 4. By keeping ϵ_{ff} fixed to 1 per cent, while varying n_0, we observe a strong change in the ability to form stars at large radii. The galaxies adopting a large threshold have a more concentrated distribution of stars, smaller stellar disc scalelengths as well as larger Σ_{gas} at all radii. The scalelengths are $r_d > 4$ kpc for $n_0 = 0.1\,\mathrm{cm}^{-3}$, but only $r_d \sim 2.5$ kpc for $n_0 = 1\,\mathrm{cm}^{-3}$. The latter values are on the low side when compared to observations of late-type spirals at this mass range (Courteau, de Jong & Broeils 1996; Courteau 1997; Gnedin et al. 2007). The systematically lower Σ_s signals an under-resolved or 'missing' star formation throughout the disc: the average physical gas density does not efficiently cross the targeted n_0, even at intermediate radii. This is also reflected in the gas fractions of $\sim$25 per cent, which is much larger than the observed average values for galaxies of this size (Garnett 2002; Zhang et al. 2009). The rotational velocities are large at smaller radii for $n_0 = 1\,\mathrm{cm}^{-3}$, regardless of the choice of ϵ_{ff}. Naively one would expect this numerically induced star formation

Table 2. Summary of disc characteristics at $z = 0$. The mass of the components are obtained by fitting the stellar surface density (see text), and are in units of $10^{10}\,M_\odot$. Note that we consider *all* gas phases for the gas mass and all stars for the stellar masses. (1) Fitted scalelength of stellar disc. Large uncertainties exist for $r_d > 10$ kpc as the stellar discs are small and feature almost flat stellar surface density profiles. (2) $f_{gas} = M_{disc,g}/(M_{disc,tot} + M_{bulge})$. (3) Total measured specific angular momentum of the baryons in the disc and bulge in units of km s^{-1} kpc.

| Run	$M_{disc,s}$	$M_{disc,g}$	$M_{bulge,s}$	r_d (kpc) (1)	f_{gas} (2)	B/D	B/T	j_{bar} (3)
SR6-n01e1	8.6	1.6	2.0	3.8	0.13	0.23	0.19	1920
SR6-n01e2	7.4	1.3	4.6	7.6	0.10	0.62	0.38	1655
SR6-n01e5	5.6	0.72	7.0	$\sim$15.0	0.05	1.25	0.56	1305
SR6-n01e1ML	8.0	2.3	2.2	5.0	0.18	0.27	0.21	1960
SR6-n01e2ML	8.1	1.6	3.8	5.0	0.12	0.47	0.32	1718
SR6-n01e5ML	5.5	0.93	7.2	$\sim$15.0	0.07	1.30	0.57	1464
SR6-n1e1	6.6	3.3	2.9	2.7	0.26	0.44	0.31	1594
SR6-n1e2	6.4	2.4	4.3	2.5	0.18	0.67	0.40	1804
SR6-n1e5	6.0	2.1	5.2	2.7	0.16	0.87	0.46	1643
SR6-n1e1ML	6.5	3.6	2.7	2.7	0.28	0.42	0.29	1618
SR6-n1e2ML	6.3	2.9	4.3	2.7	0.21	0.68	0.41	1281
SR6-n01e1NFB	7.8	1.6	3.1	4.0	0.13	0.40	0.28	1938
SR6-n01e5NFB	5.8	0.62	6.5	$\sim$15.0	0.05	1.12	0.53	1394
SR6-n01e5NFBmet	5.6	0.56	6.6	10.0	0.05	1.18	0.54	1430
SR6-n01e5SN2	5.6	0.55	6.5	4.5	0.05	1.16	0.54	1266
SR6-n01e5SN5	6.6	0.81	2.3	2.8	0.09	0.35	0.26	1387
SR5-n1e1ML	9.0	2.0	2.2	2.8	0.18	0.24	0.20	
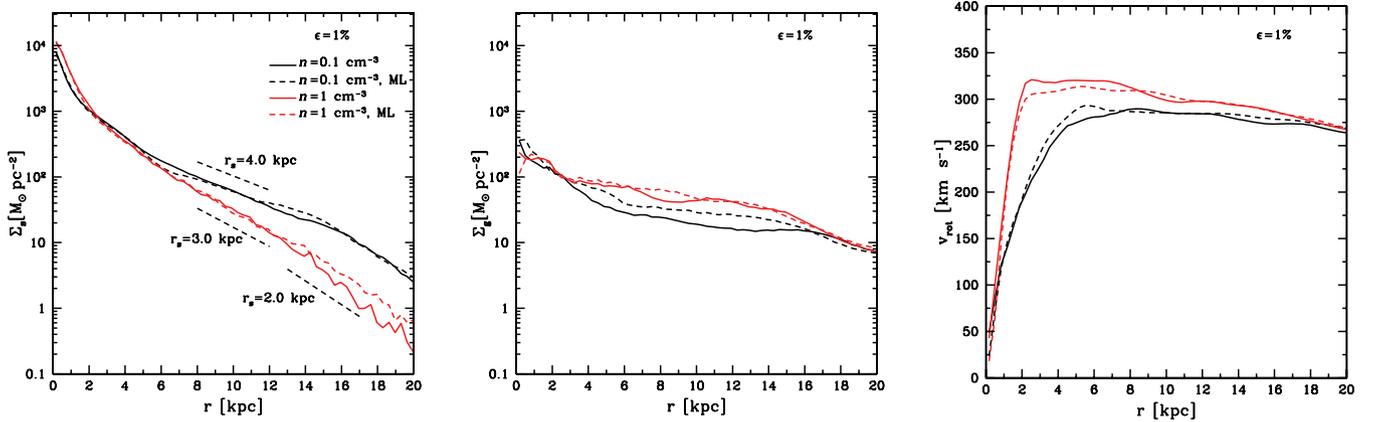
Figure 4. The effect of the Schmidt-law star formation density threshold. The panels show the stellar surface density (left), gas surface density (middle) and rotational velocity measured from the gas (right). We consider all material within a height of $|z| < 2.5$ kpc for all components. The star formation efficiency is $\epsilon_{ff} = 1$ per cent in all simulations. The different colours are described in the first panel, and a dashed line indicates that we use the extended feedback model (see text).
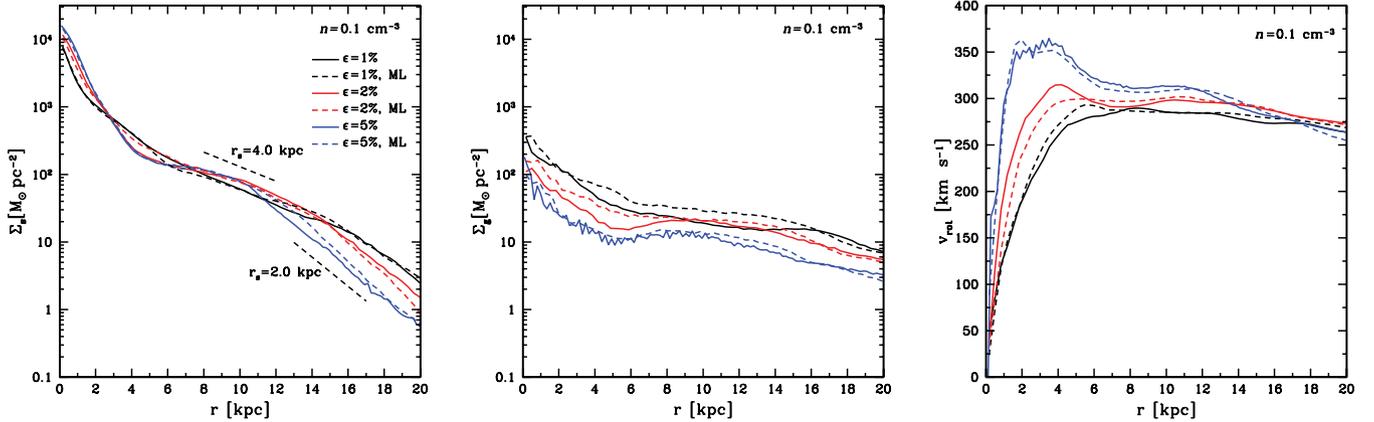
Figure 5. The effect of the Schmidt-law star formation efficiency. The panels show the stellar surface density (left), gas surface density (middle) and rotational velocity measured from the gas (right). We consider all material within a height of $|z| < 2.5$ kpc for all components. The Schmidt-law density threshold is $n = 0.1$ cm^{-3} in all simulations. The different colours are described in the first row, and a dashed line indicates that we use the extended feedback model (see text).

deficiency to alleviate the angular momentum loss at high redshift, hence forming a less concentrated galaxy. However, due to disc secular evolution this is not the case: disc instabilities drive gaseous flows to the centre of the disc where, as the gas crosses the correct threshold, star formation can proceed. We conclude, that given our numerical resolution and simulated system, $n_0 = 0.1$ cm^{-3} yields more realistic (average) disc galaxies when compared to observations. We discuss this numerical effect and its relationship to the adopted mesh resolution further in Appendix B. Note that this is not a fundamental result of galaxy formation, but serves only as tuning given our numerical resolution and is a basis for the subsequent tests. As discussed in Section 2.1, n_0 should be increased as the resolution is increased.

5.2 The star formation efficiency, ϵ_{ff}

We now turn to the data presented in Fig. 5, where we keep the threshold fixed at $n_0 = 0.1$ cm^{-3} and adopt $\epsilon_{ff} = 1$, 2 or 5 per cent. As ϵ_{ff} is increased, Σ_{star} increases at small radii i.e. the bulge mass increases, signalling a lower disc angular momentum. The B/D ratio increases from 0.25 to 1.25 as ϵ_{ff} increases from 1 to 5 per cent. Σ_{gas} roughly follows a $1/r$-profile and the magnitude is lowered at all radii by approximately the relative change in efficiency. The stellar

disc is less extended and the exponential scalelength increases for larger efficiencies (see Table 2). For $\epsilon_{ff} = 1$ per cent, the disc scalelength is measured to be $r_d \sim 4$–5 kpc, in good agreement with observed average values from the SDSS (Gnedin et al. 2007), while for $\epsilon_{ff} = 5$ per cent, $r_d \approx 15$ kpc is a $>2\sigma$ outlier. Large uncertainties exist for $r_d > 10$ kpc as the stellar discs are small and feature almost flat stellar surface density profiles.

At large radii in all simulations, r_d shifts to ~ 2 kpc. Disc breaking is a well-observed phenomenon (Pohlen & Trujillo 2006) correlated with a dip in the star formation rate, and has been studied numerically by Roškar et al. (2008). As larger star formation efficiencies lead to less extended discs, the disc breaks occur at smaller radii: $r_{break} \approx 16$, 14, 10 kpc for $\epsilon_{ff} = 1$, 2 and 5 per cent, respectively. The breaks can also be seen from the average stellar ages $\langle t_* \rangle$, shown in Fig. 6. The central parts of the discs generally consist of older stars formed at $z > 1$, and $\langle t_* \rangle$ decreases with larger radii, reaching $\langle t_* \rangle \approx 6$ Gyr. Past the disc break, older stars appear which in part can be attributed to stellar migration as well as pollution by old halo stars with $\langle t_* \rangle \approx 11$–12 Gyr. We note that $\langle t_* \rangle$ flattens or even declines towards the centre of the discs as ϵ_{rmff} is lowered. This is due to secular evolution: as spiral structure is more pronounced (as in n01e1), gas is transported towards the centre more efficiently and late-time star formation occurs; see Fig. 1.
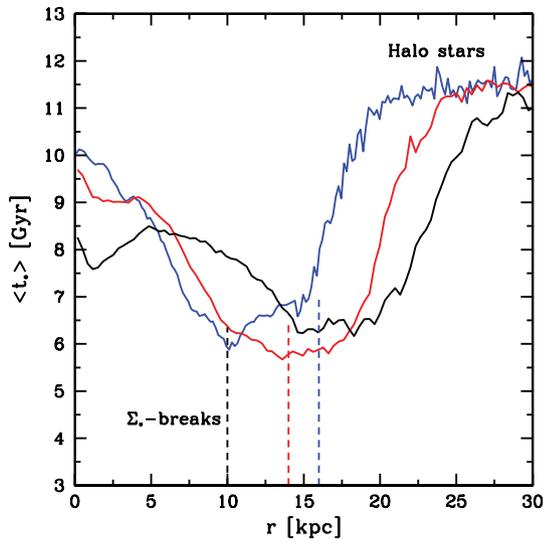
Figure 6. Average stellar ages as a function of radius. The colours represent different star formation efficiencies, $\epsilon_{\rm ff} = 1$ (black), 2 (red) and 5 per cent (blue). Dashed lines mark the measured stellar surface density breaks.

The efficiency has a strong impact on the rotational velocity. The rotation curve in the n01e5 simulation features a strong peak in the inner parts of the disc. As $\epsilon_{\rm ff}$ is lowered, B/D decreases and the velocity profile flattens. Only when $\epsilon_{\rm ff} < 2$ per cent can a flat rotational velocity profile be produced! In n01e1, the rotational velocity reaches $v_{\rm rot} \approx 275\,{\rm km\,s^{-1}}$ and stays roughly flat. For n01e2 and n01e5, $v_{\rm rot}$ peaks at ≈ 310 and $360\,{\rm km\,s^{-1}}$, but converges at $275\,{\rm km\,s^{-1}}$ close to $r = 20$ kpc.

In the left-hand panel of Fig. 7, we plot the *circular* velocities, i.e. $v_{\rm c}(r) = \sqrt{GM(<r)/r}$, for the dark matter, disc + bulge baryons and total mass of the galaxies. We note that the $v_{\rm c}$-profiles are well traced by the cold gas rotation curve (the stellar rotational velocities are lower than what can be expected from $v_{\rm c}$ due to a larger velocity dispersion). While all simulations converge at large radii, and have an equal dark matter and baryon contribution within $r \sim 17$ kpc, the mass distribution (and angular momentum distribution) differs dramatically leading to a large difference in circular velocities. As we will demonstrate in the next section, a majority of the mass within the bulge component originates from the intense star formation epoch at $z \sim 2$–3 where the value of $\epsilon_{\rm ff}$ matters the most. We also observe a significantly enhanced dark matter contraction at large $\epsilon_{\rm ff}$. This effect in our simulation suite, and its relevance for direct dark matter detection, has recently been analysed by Pato et al. (2010).

5.3 Star formation histories

The left-hand panel of Fig. 8 shows the star formation histories for all stars belonging to the discs in n01e1, n01e2 and n01e5 at $z = 0$. The average SFR at the current epoch is $\sim$3–4 $M_\odot\,{\rm yr^{-1}}$ in all simulation, regardless of numerical setting. Moreover, the star formation history during the quiescent phase of disc evolution, i.e. after $z \sim 1$, is relatively flat and roughly the same in all simulations. Significant differences occur at intense epochs of star formation, especially at $z = 3$ where the proto-disc is assembled via cold streams, satellite mergers and gas accretion from the hot halo, as seen in the

simulation snapshot in Fig. 9.[2] Here the peak of SFR changes dramatically from $\sim$43 $M_\odot\,{\rm yr^{-1}}$ in n01e5 to $\sim$23 $M_\odot\,{\rm yr^{-1}}$ in n01e1.

In n01e5, stars form efficiently everywhere, even in satellites. The gas is quickly consumed locally during the high-redshift assembly, and merging systems lose angular momentum to the dark halo, ending up in the central part of the galaxy. Accretion via cold streams and from the hot gaseous halo will still supply the galaxy with unprocessed gas (Agertz et al. 2009; Dekel et al. 2009), but now in a more bulge-dominated environment. In n01e1, star formation is less efficient and a significant portion of the mass in the merging clumps is in gaseous form. This material is lost to the hot gaseous halo via ram-pressure and tidal stripping, or expelled during SNe events, which later cools down to join the disc. Hence, the material that is not consumed by star formation at $z = 3$ is processed at a later epoch, closer to $z = 1$–2 (see Fig. 8), but now in a more disc-like, higher angular momentum configuration. In fact, the trend at $z = 3$ is reversed at this later epoch, and the largest SFR is found for $\epsilon_{\rm ff} = 1$ per cent. These two modes of star formation are related to the classical angular momentum problem (Navarro & White 1994), and they lead to fundamentally different modes of disc assembly and morphology.

A confirmation of the above discussion is shown in Fig. 10, where contours of formed stellar masses are outlined in the star formation time-disc radius plane. Note that this mass refers to all the stars at $z = 0$ contained in the disc, and is hence the sum of the stars formed in merging satellites as well as in situ. While the formed stellar mass in n01e1 is smoothly distributed in a roughly exponential profile across the disc at all times, without a clear sign of extreme star formation bursts, the n01e5 simulation shows a strong central concentration of stars formed at $t = 11.5$ Gyr ($z \sim 3$). This analysis confirms the notion of efficient star-forming satellites losing angular momentum and being dragged into the central parts of the galaxy.

5.4 Hubble types

Fig. 1 shows mass-weighted projections of the stellar and gas surface densities for n01e1ML, n01e1, n01e2ML, n01e2, n01e5ML and n01e5. The gaseous discs are thin and extended in all simulations, and are surrounded by a warped layer of cold/warm gas, probably associated with misaligned accretion events (Shen & Sellwood 2006). A hot gaseous halo surrounds the discs, and a temperature projection (not shown) reveals an extended disc–halo interface of warm/hot gas. We will explore this in future work.

As discussed in Section 5.2, we find a very strong trend in disc and bulge mass with increasing star formation efficiency. The n01e1 simulation features a $8.6 \times 10^{10}\,M_\odot$ stellar disc with a $2 \times 10^{10}\,M_\odot$ bulge, hence B/D $\sim 1/4$. In n01e5 the disc is 35 per cent less massive and the bulge 3.5 times more massive with B/D ~ 1.25. Roughly the same scaling holds when including additional SNIa feedback and stellar mass-loss.

All discs show spiral pattern in the gas component with a larger amplitude in the more gas-rich discs, having lower $\epsilon_{\rm ff}$. We also observed spiral structure in the stellar component also, which is the

---

[2] The image is an *RGB* composite image where *red* is temperature, *green* is metals and *blue* is density. Each quantity is a mass-weighted average along the line of sight. For each image pixel, we calculate the *RGB* triplet as

$$(R, G, B) = 255 \left[\frac{\log(T/T_{\rm m})}{\Delta T}, \frac{\log(Z/Z_{\rm m})}{\Delta Z}, \frac{\log(\rho/\rho_{\rm m})}{\Delta \rho} \right],$$

where $\log T_{\rm m}\,({\rm K}), Z_{\rm m}(Z_\odot), \rho_{\rm m}\,({\rm cm^{-3}}) = 4.1, -3, -4.8$ and $\Delta T, \Delta Z, \Delta \rho = 2, 2, 6$.
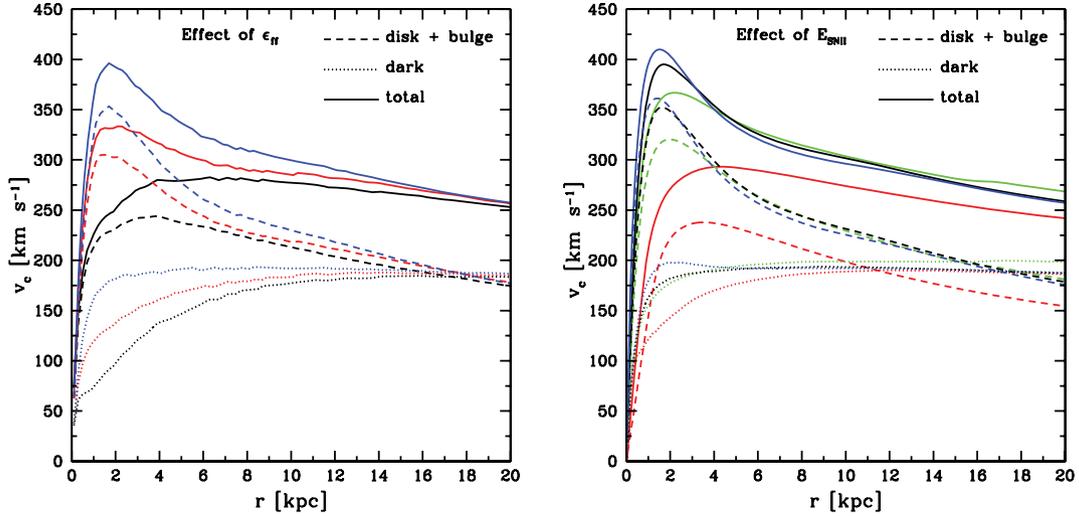
Figure 7. Circular velocities, $v_c = \sqrt{GM(<r)/r}$, of the stars (solid), dark matter (dotted) and total mass (dashed). (Left) The effect of the star formation efficiency: $\epsilon_{ff} = 1$ (black), 2 (red) and 5 per cent (blue). (Right) The effect of supernovae feedback strengths (adopting $\epsilon_{ff} = 5$ per cent): $E_{SNII} = 0$ (blue), 10^{51} erg (black), 2×10^{51} erg (green) and 5×10^{51} erg (red).
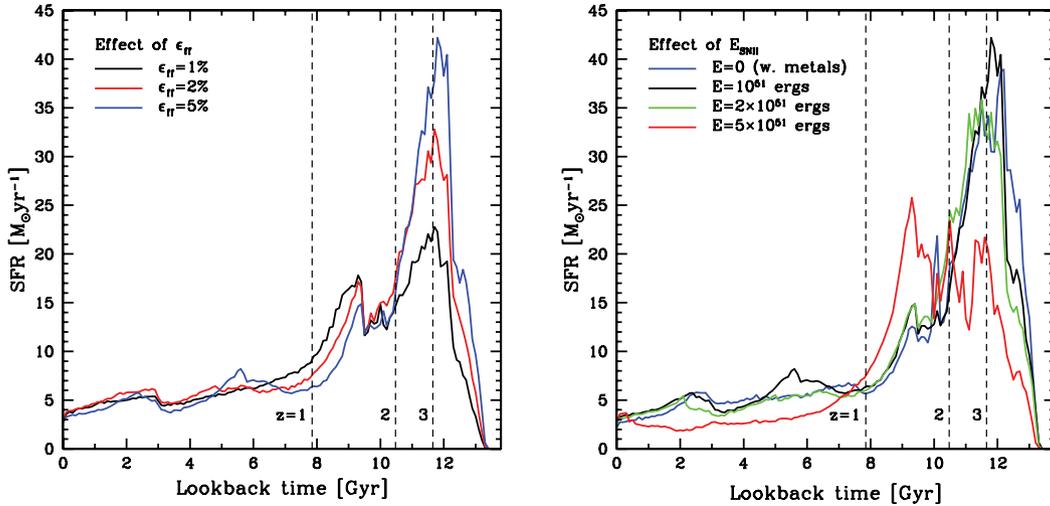

Figure 8. (Left) Star formation histories using different values of ϵ_{ff}. At $z < 1$, all simulations regulate to similar SFRs, ending up at ~ 3–$4 \, M_\odot \, yr^{-1}$ at $z = 0$, regardless of star formation parameters. Using a high efficiency leads to central galaxies and dwarfs burning their fuel quickly at high redshift during galaxy assembly, resulting in excess angular momentum loss and a prominent central spheroid. A lower efficiency avoids this issue, leaving more gas for star formation at lower redshifts in a more disc-like configuration. (Right) Star formation histories for a set of simulations of increasing supernovae feedback strength (E_{SNII}). We note that the large SFR peak at $z = 3$ is only lowered when a very large amount of energy is injected into the ISM.

most pronounced in n01e1 and n01e1ML and n01e2ML simulations. As ϵ_{ff} is increased, B/D increases and the spiral arms become more tightly wound as marginal gravitational instabilities can no longer excite pronounced open spiral arm structure. All discs feature a stellar bar, and viewed edge-on, we observe how the inner stellar distribution flattens as ϵ_{ff} is decreased. The flattened central parts of n01e1 and n01e1ML, and the fact that the bulge is well fitted using an exponential, is indicative of a bulge formed via secular processes (Kormendy & Kennicutt 2004) e.g. bar buckling (Debattista et al. 2006). The gaseous bar strengthens at lower ϵ_{ff}, and in n01e1 and n01e1ML gas is transported towards the disc centre, triggering star formation. In these simulations, close to 50 per cent of the stars associated with the bulge formed in situ in the disc at $z \lesssim 1$, and only ~ 25 per cent formed at the intense star formation peak at $z \sim 3$. This indicates that a significant portion of the flattened bulge has formed via secular evolution, leading to a pseudo-bulge. This

is in stark contrast to the bulge formation epoch seen in the central parts of the n01e5 simulations (right-hand panel of Fig. 10), where essentially all bulge stars form at $z \sim 3$.

Weinzirl et al. (2009) (see also Laurikainen et al. 2010), recently analysed 182 *H*-band images from the OSUBSGS survey (Eskridge et al. 2002) to obtain B/D and B/T values across the Hubble sequence. Comparing their sample averages (see e.g. their fig. 14) to our set of simulations (B/D in Table 2) suggests that the final disc in n01e5 is of S0/a type, in n01e2 it is of Sa/Sab type and in both n01e1 and n01e1ML it is of Sb/Sbc type. We consider this agreement only as indicative as each Hubble type spans a wide range of B/D and B/T values. Graham & Worley (2008) presented B/D and B/T flux ratios using a sample of over 400 galaxies observed in the *K* band. Their B/D estimates for different Hubble types confirm the classification of our simulated discs. There is no doubt that we are measuring a transformation along the Hubble sequence.
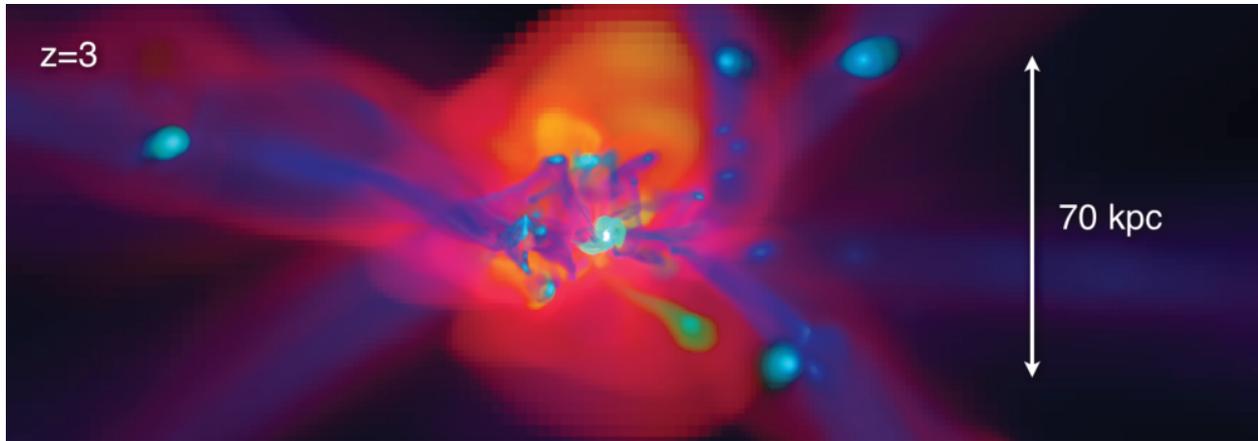
Figure 9. A large-scale view of the assembling spiral galaxy from the SR5 simulation at $z \sim 3$; the most intense epoch of star formation for this system. The *RGB*-image[2] shows the gas component using temperature (red), metals (green) and density (blue). We can clearly distinguish accretion via streams of cold pristine gas (in blue) penetrating the shock-heated gas (in red), reaching the heart of the halo. Dwarf galaxies outside of the large gaseous halo are surrounded by puffy distributions of enriched gas originating from stellar outflows. Gas is efficiently lost via tidal and ram-pressure stripping as the dwarfs interact with the main galaxy and its hot gaseous halo. The distance measure is in physical units.
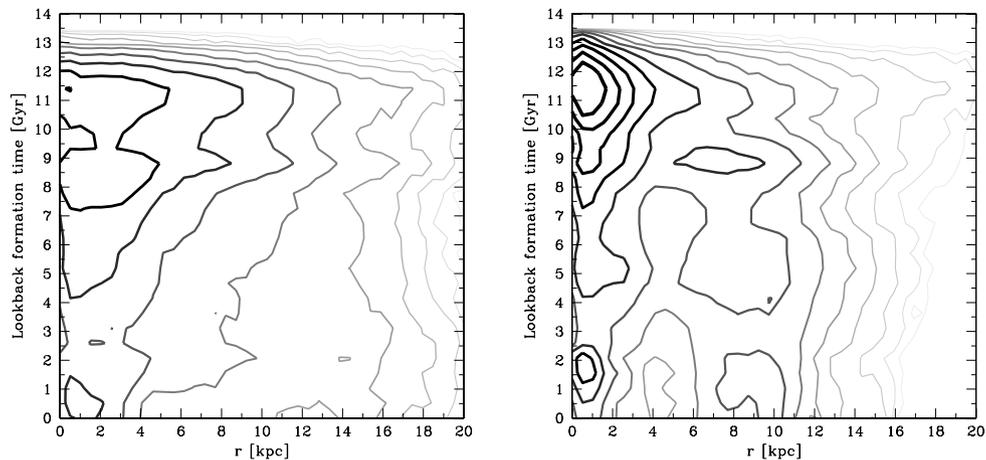

Figure 10. Formation time of stars and their radial distribution for the discs in n01e1 (left) and n01e5 (right) at $z = 0$. The contours trace regions of binned mass using bins of size $\Delta t = 0.5$ Gyr and $\Delta x = 0.5$ kpc. The contour lines trace, from thin lines with light shades, to thick lines with dark shades, the formed stellar masses from $\log (M_*) = 6.5$ to $\log (M_*) = 9.5$ in steps of 0.25 dex. While the formed stellar mass in n01e1 is smoothly distributed across the disc at all times, the n01e5 simulation shows a strong central concentration of stars formed at $t = 11.5$ Gyr ($z \sim 3$).

6 EFFECT OF SUPERNOVA FEEDBACK

As we have demonstrated in the previous sections, a high SFE overproduces the central stellar mass of the galaxy. The inclusion of additional SNIa feedback and stellar mass-loss did not drastically change the galaxy properties, even though differences can be seen in Fig. 1 (the discs in n01e1 and n01e2 feature much stronger spiral structure) and Fig. 4, and more late time star formation is made possible (see Section 7.2). The effect of stellar mass-loss was studied by Martig & Bournaud (2010) who found a stronger effect on the bulge mass in a similar setting, perhaps due to implementation differences.

In Figs 7 and 11 we present v_c and Σ_s for the n01e5 simulation, but with different amounts of injected SNII energies; see Table 2. Note that we still enrich the ISM with metals in the simulation with $E_{SNII} = 0$. Without this, the effect of metal cooling will not be present in all simulations. We find that the bulge mass is lowered as we increase E_{SNII}, but only for a very large injected value of 5×10^{51} erg can the disc rotation curve peak at a reasonable

$v_c < 300$ km s^{-1}, resembling that of the n01e1 simulation. As for the standard feedback runs in the previous section, the dark matter halo is more contracted as star formation is less regulated. The difference in v_c at $r = 20$ kpc between the n01e5SN5 and the other simulations, corresponding to a few 10^{10} M$_\odot$, is due to the expelled gas during galaxy assembly which can be accounted for in the more massive gas halo. This effect can also be seen in Σ_s as the central values are decreased, the discs scale radius decreases and the break radius is shifted to larger radii. As seen in Table 2, a massive disc still forms. The effect on the star formation histories is shown in the right-hand panel of Fig. 8; we find no significant difference among the simulations, apart for the very energetic n01e5SN5 simulation. The SFH now resembles that of n01e1 where the $z = 3$ amplitude is lowered to ≈ 20 M$_\odot$ yr^{-1} and more gas is left to form stars in a disc-like environment at $z \sim 1$–2.

The projected gas density and stellar maps were shown in Fig. 2. While the standard feedback simulations shown in Fig. 1 showed a clear Hubble sequence of open to tightly wound spiral structure as B/D was lowered, this is not the case for the feedback test suite. In
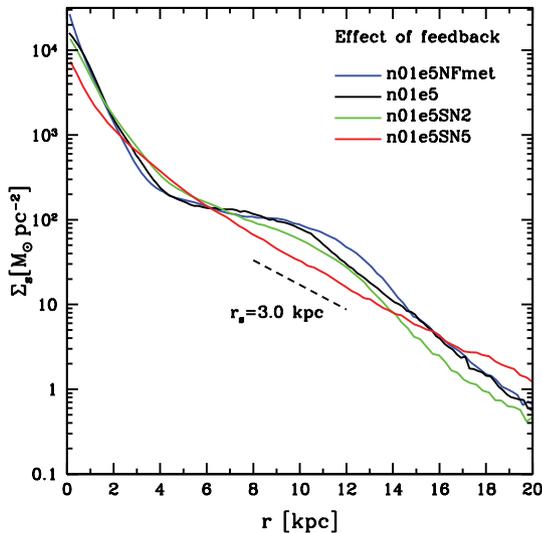
Figure 11. Stellar surface densities of the $z = 0$ discs in the supernova feedback test suite. As the SNII feedback energy input is increased, the disc becomes more extended and the bulge component less massive.

n01e5SN5, the gaseous disc is heavily distorted, warped and puffed up by the large SNII energy injections. Star formation is here very different compared to n01e1 as stars form in filaments and shells from SNe explosions rather than in gas-rich spiral arms.

The effect of metal cooling is not always accounted for in cosmological simulations. Piontek & Steinmetz (2009a) included this effect and reported on difficulties in suppressing the initial high-z peak, even with sophisticated feedback models. In our simulations metal cooling is roughly counteracted by the standard SNII feedback. If metal enrichment is turned off together with the feedback, we do not find a significant modification to our discs. For example, the n01e1NFB simulation shows a surprisingly successful set of characteristics when compared to n01e1 (see Table 2). As a zero-metallicity gas cools inefficiently below 10^4 K, as well as in the range 10^5–10^7 K, the n01e1NFB disc essentially behaves as a higher metallicity counterpart but with SNII heating balancing cooling. This is the philosophy behind subgrid multiphase models (e.g. Springel & Hernquist 2003) in which feedback is implicitly treated as a stiff gas equation of state. Note that our polytropic EOS is slightly stiffer than what is usually adopted ($\gamma = 2$ instead of $\gamma = 5/3$).

7 RELATIONSHIP TO OBSERVATIONS

7.1 Angular momentum of the baryons

For each galaxy we calculate the cumulative specific angular momentum vector, defined as

$$\boldsymbol{j}_{\mathrm{bar}}(\leq r) = \frac{1}{M(\leq r)} \sum_{i=1}^{N(\leq r)} m_i \boldsymbol{x}_i \times \boldsymbol{v}_i, \qquad (11)$$

including all bulge and disc baryons. Here $\boldsymbol{x}_i$ and $\boldsymbol{v}_i$ are positions and velocities of the gas cells and star particles of the N elements within a radius r encapsulating the mass $M(\leq r)$. The resulting $j_{\mathrm{bar}} = |\boldsymbol{j}_{\mathrm{bar}}|$ are presented in Table 2.

Using the sample of Courteau (1997) and Mathewson, Ford & Buchhorn (1992), Navarro & Steinmetz (2000) calculated the specific angular momenta versus rotational velocity for late-type spiral galaxies and compared them to numerical simulations. The discs

were assumed to follow an exponential profile for which the peak rotational velocity, $v_{\mathrm{rot,2.2}}$, occurs at $r = 2.2r_{\mathrm{d}}$, and it follows that $j_{\mathrm{bar}} = 2r_{\mathrm{d}}v_{\mathrm{vrot,2.2}}$. This assumption can be misleading when comparing to simulated galaxies as the true v_{rot}-peak can be significantly underestimated in the case of bulge-dominated disc galaxies. The sample of Courteau (1997) concerned Sb-Sc galaxies for which B/D is low and a dominating exponential disc assumption is roughly valid. The difference in measured and estimated angular momentum content makes it difficult to compare simulated and observed galaxies, as discussed in Abadi et al. (2003a) and Piontek & Steinmetz (2009b). A simulated galaxy can be considered as a successful realization of a late-type (Sb-Sc/Sd) galaxy if the estimated and measured angular momenta are in agreement.

Focusing on the $n = 0.1$ cm^{-3} suite, we find that the n01e1 and n01e1ML simulations are in good agreement with the observed galaxies, both when analysed using equation (12) and the exponential disc approximation. Typical measured and estimated values are here $j_{\mathrm{bar}} \sim 2000$ km s^{-1} kpc and $j_{\mathrm{bar}} \sim 2750$ km s^{-1} kpc, respectively. As ϵ_{ff} is increased, the calculated angular momentum decreases. The $\epsilon_{\mathrm{ff}} = 2$ per cent simulations are still a part of the observed scatter while higher values create more significant outliers in the observed distribution. When using the exponential disc approximation, all simulated galaxies are in good agreement with the observed data as the velocities are quite comparable at larger radii, and for the fact that the discs, although less extended, have larger r_{d} in the higher-efficiency cases (see Fig. 5). We conclude that an angular momentum reservoir comparable to Sb/Sc galaxies has been reproduced for the baryons in the case of low SFE (i.e. $\epsilon_{\mathrm{ff}} = 1$ per cent).

The lack of correlation between E_{SNII} and the baryonic angular momentum content might come as a surprise. However, while the B/D ratio decreases for large supernova energy injections, the actual disc mass changes little, and is $\sim 6 \times 10^{10}$ M$_\odot$ for all $\epsilon_{\mathrm{ff}} = 5$ per cent simulations. As the net contribution of the bulge to the angular momentum content is roughly zero, similar j_{bar} is to be expected. All $\epsilon_{\mathrm{ff}} = 5$ per cent simulations have measured $j_{\mathrm{bar}} \sim 1300$–$1450$ km s^{-1} kpc which is close to the estimated $j_{\mathrm{bar}} \sim 1600$ km s^{-1} kpc in n01e5SN5.

In summary, the largest measured baryonic specific angular momentum reservoir can be found in simulations using $\epsilon_{\mathrm{ff}} = 1$ per cent due to a massive disc component, regardless of including feedback or not. At higher efficiencies, j_{bar} decreases, again regardless of feedback.

7.2 The Tully–Fisher relationship

The photometric Tully–Fisher (TF) relation (Tully & Fisher 1977) links the characteristic rotational velocity of a galaxy with its total absolute magnitude. This correlation holds in all typical photometric bands but with variation in functional form (e.g. Pizagno et al. 2007). Early attempts in forming realistic galaxies (e.g. Abadi et al. 2003a) showed off-sets in the observed relation owing to the formation of very concentrated bulge-dominated galaxies with a low star formation activity at late times. Their velocity–magnitude relation had more in common with S0 galaxies (Mathieu, Merrifield & Kuijken 2002). Recent work seems to have improved on these results by SN feedback regulated star formation (Governato et al. 2007; Piontek & Steinmetz 2009b). These studies place galaxies closer to the observed relation, but this is in part achieved by circumventing the large measured v_{rot} (caused by the dominant bulge) by using the exponential disc assumption discussed above (but see Governato et al. 2009), i.e. using $v_{\mathrm{rot,2.2}}$. Observationally, the
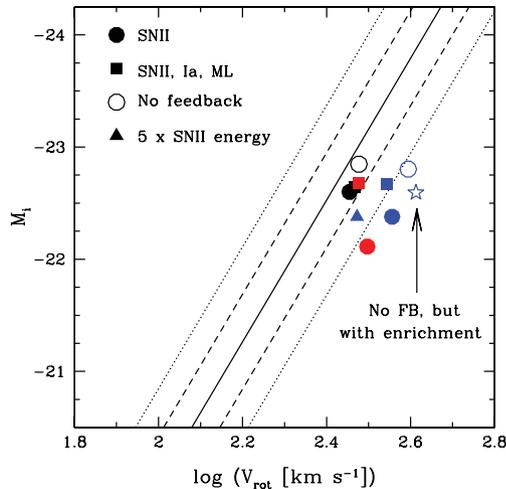
Figure 12. The *i*-band Tully–Fisher relationship from the SDSS (Pizagno et al. 2007). We show the observed average (solid line), 1σ (dashed line) and 2σ (dotted line) relation. The symbols are results from our simulated galaxies, which use $n_0 = 0.1\,\mathrm{cm}^{-3}$ and $\epsilon_{\mathrm{ff}} = 1$ (black symbols), 2 (red symbols) and 5 (blue symbols) per cent.

measured quantity is often half of the HI velocity width at $20(W_{20})$ or $50(W_{50})$ per cent of the peak intensity.

In Fig. 12 we present the measured *i*-band magnitudes of several of our simulated galaxies as a function of their peak rotational velocities measured from the gas component. These are compared to the observed T–F relation from the SDSS (Pizagno et al. 2007). Pizagno et al. measured the velocity at a radius containing 80 per cent of the *i*-band flux. This measure (V_{80}) is equivalent to measuring v_{rot} at $\sim 3r_{\mathrm{d}}$ for a pure exponential disc. By using the true peak of v_{rot}, we provide an absolute lower limit to the agreement with observations, and can clearly separate disc- and bulge-dominated galaxies. We note that the low-efficiency models agree well with the average data, regardless of adopted feedback scheme, and even without. At higher efficiencies, the discs are off-set by more than 2σ, mostly due to their peaked rotation curves. In these circumstances, the inclusion of additional recycling via SNIa and stellar mass-loss increases the magnitudes by ~ 0.5 dex in n01e2ML and n01e5ML simulations. The n01e5NFB simulation is brighter than the corresponding simulations including feedback due to exclusion of metal enrichment, leading to less efficient cooling and more gas left to form stars at later times. Allowing for enrichment without any energy deposition demonstrates this fact (see figure). From a photometric T–F point of view, the $\epsilon_{\mathrm{ff}} = 5$ per cent discs correspond to S0 systems or early-type spirals (Mathieu et al. 2002).

As described in the previous sections, v_{rot} and Σ_{s} in the n01e5SN5 simulation agree fairly well with the disc values found in n01e1. The strong feedback brings the galaxy closer to the observed values but the absolute magnitude is still lower than in the $\epsilon_{\mathrm{ff}} = 1$ per cent simulations. The SFH in Fig. 8 tells us why: after $z = 1$ the SFR is lower in n01e5SN5 compared to n01e1 by almost a factor of 2 (even though the $z = 0$ values agree) due to strong gas expulsion, resulting in a less bright disc by $\sim 1/3$ dex in *i*-band magnitude.

As for the specific angular momentum analysis, adopting the $v_{\mathrm{rot,2.2}}$ measure (or V_{80}), *all* discs would agree statistically with the observed T–F relation, especially when including SNIa feedback and stellar mass-loss.

Similar to the photometric T–F is the baryonic T–F relation (McGaugh et al. 2000, 2010) which links characteristic rotation velocity with total galaxy baryonic mass. The baryonic T–F relation therefore accounts for the fact that less massive galaxies are more gas rich, and their stars only account for a small fraction of the total disc mass. The same conclusion as above holds for the baryonic T–F: the low-efficiency simulations agree well with the observations. As the baryonic masses for the discs are not strongly affected, even in the case of extreme feedback (n01e5SN5) the data points shift only with the increase of the v_{rot} peak. As for the photometric T–F, using $v_{\mathrm{rot,2.2}}$ puts all galaxies on the observed relation.

7.3 The $\Sigma_{\mathrm{SFR}} - \Sigma_{\mathrm{gas}}$ relation

The most famous study of the globally averaged relationship between the star formation rate and gas surface density is from Kennicutt (1998) (from now on K98), where a sample of 61 nearby normal spiral galaxies and 36 infrared-selected starburst galaxies were considered. Assuming a Schmidt law of the form

$$\Sigma_{\mathrm{SFR}} = a \left(\frac{\Sigma_{\mathrm{gas}}}{1\,\mathrm{M}_\odot\,\mathrm{pc}^{-2}} \right)^N , \tag{12}$$

the full sample yielded $a = (2.5 \pm 0.7) \times 10^{-4}$ and $N = 1.40 \pm 0.15$. The $\Sigma_{\mathrm{SFR}} - \Sigma_{\mathrm{gas}}$ relation has been studied by many authors (e.g. Wong & Blitz 2002; Misiriotis et al. 2006; Kennicutt et al. 2007; Schuster et al. 2007), both locally and globally, using different star formation tracers and galaxy samples. A large range of power-law indices ($N \approx 1$–3) has been found, suggesting that either different SF laws exist in different galaxies or N is very sensitive to systematic differences in methodology. Bigiel et al. (2008) presented a comprehensive analysis of the $\Sigma_{\mathrm{SFR}} - \Sigma_{\mathrm{gas}}$ relationship using multifrequency data of seven spiral galaxies and 11 late-type and dwarf galaxies. The analysis pointed to a great variation within the sample and a markedly different functional behaviour in atomic- and molecular-dominated gas.

The THINGS data of Bigiel et al., relevant for spirals, as well as the K98 law (equation 12), is reproduced in the left-hand panel in Fig. 13 together with the azimuthally averaged ($\Delta r = 540$ pc) data from n01e1, n01e2 and n01e5. For the calculation of Σ_{SFR} we only consider stars younger than 50 Myr. At a given value of Σ_{gas} we find a clear trend of higher Σ_{SFR} values for higher ϵ_{ff}. All simulations fall on to the range of observed values, having the same functional behaviour but with an off-set. We note that only the disc in the n01e5 simulations is compatible with the K98 relation. The n01e1 simulation is on the low side but can still statistically be associated with one of the THINGS spiral galaxies. However, at high redshift the argument can be reversed, as can be seen in the right-hand panel of Fig. 13. The observations of DLAs at $z \sim 3$ by Wolfe & Chen (2006) are typically an order of magnitude lower than the K98 relation, agreeing only with measurement of the low-density environment of the discs in our low-efficiency simulations. This trend is also predicted by simulations including treatment of H_2 formation (Gnedin & Kravtsov 2010a,b). In essence, while n01e1 is on the low side at $z = 0$, it is consistent with high-redshift observations and the reverse argument is valid for n01e5. A higher efficiency is acceptable at lower redshift, and is predicted due to e.g. higher gas metallicity. As the bulge component is assembled at high redshift, the efficiency of star formation during this epoch is crucial in setting the morphology of the galaxy.

The same analysis is performed for the feedback test suite in Section 6, and shown in Fig. 14. At $z = 0$, all simulations show a similar functional behaviour, but with a weak trend of lower Σ_{SFR} as E_{SNII} is increased, while remaining comparable to the K98

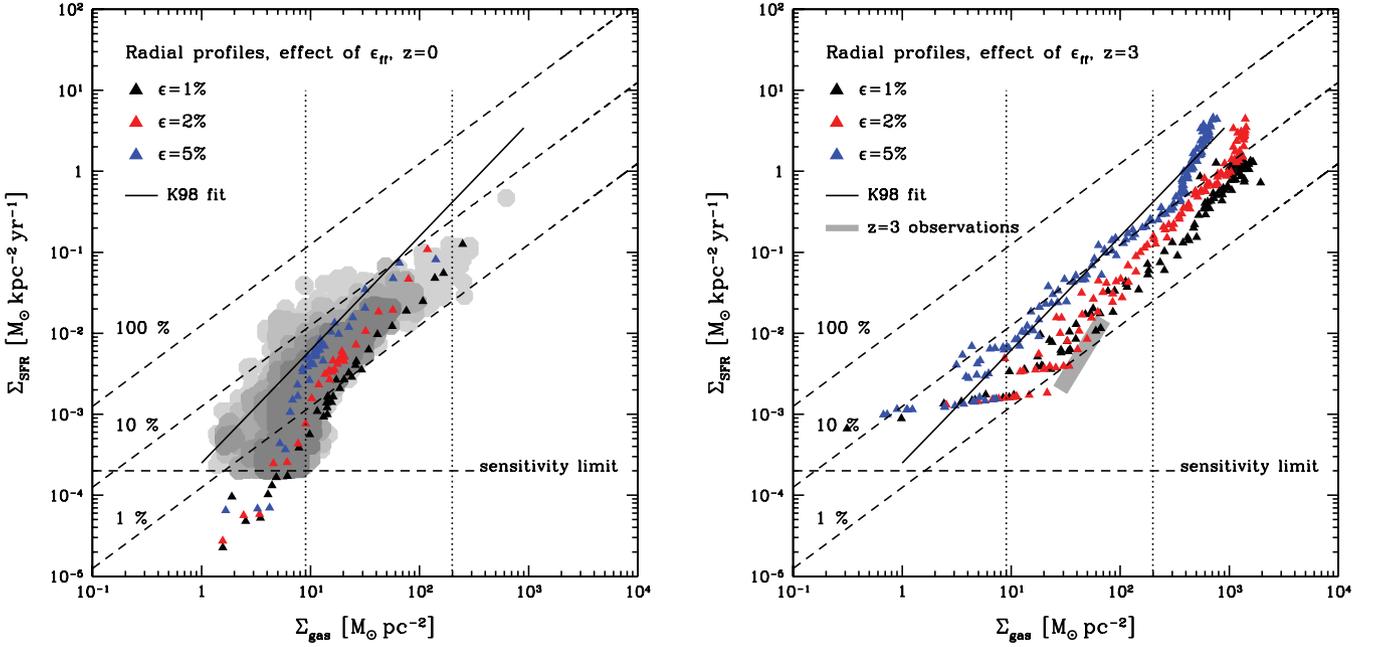**Figure 13.** Σ_{SFR} versus Σ_g for the resulting discs using $\epsilon_{ff} = 1$ (n01e1), 2 (n01e2) and 5 (n01e5) per cent at $z = 0$ (left-hand panel) and at $z = 3$ (right-hand panel). The filled circles are radial data for seven spiral galaxies from the THINGS survey (Bigiel et al. 2008), where Σ_{gas} includes the contribution from helium ($\Sigma_{gas} = 1.36\,\Sigma_{HI+H_2}$). The data points represent, from lightest to darkest, >1, >5, >10, >20 and >30 detections. The vertical dotted lines separate regions where different star formation laws are conjectured to apply (see text). Diagonal dotted lines show lines of constant $SFE = \Sigma_{SFR}/\Sigma_{gas}$, indicating the level of Σ_{SFR} needed to consume 1, 10 and 100 per cent of the gas reservoir in 10^8 yr. The solid black line is the average relation from Kennicutt (1998). The $z = 3$ observations approximately populate the region of the Wolfe & Chen (2006) observations. THINGS data courtesy of F. Bigiel.
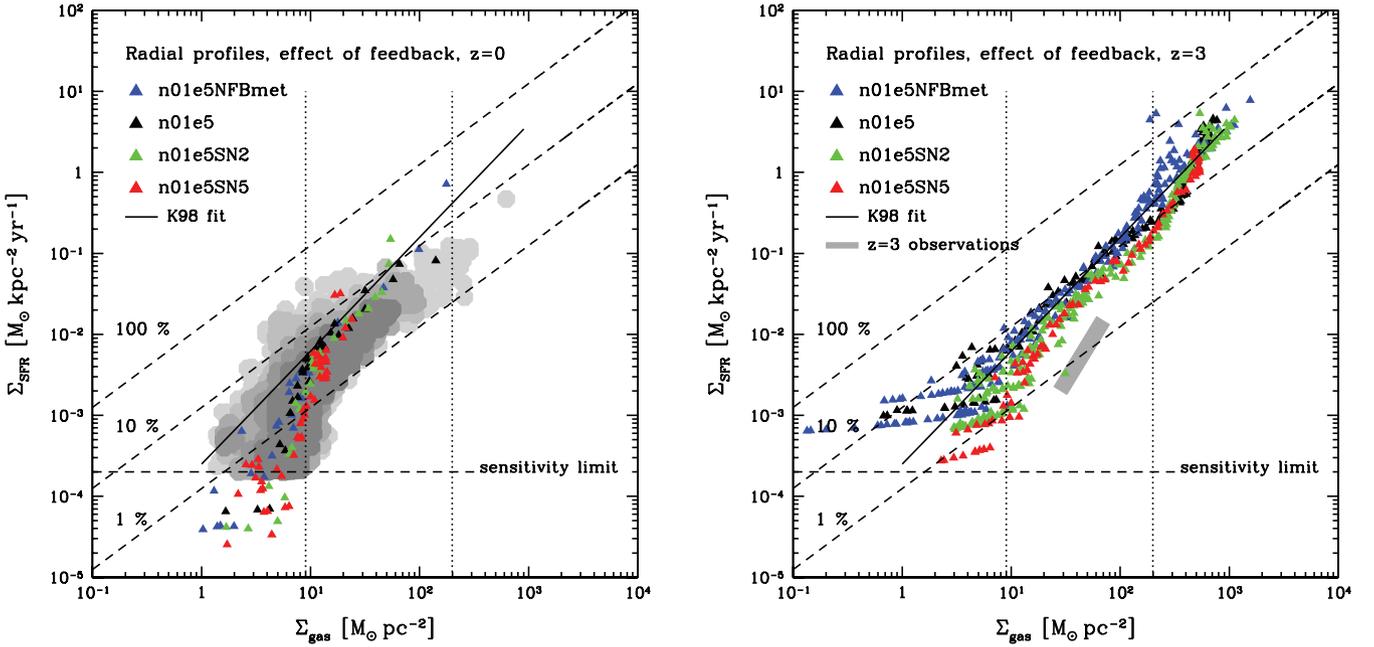

Figure 14. Σ_{SFR} versus Σ_g for the resulting discs using a high star formation efficiency ($\epsilon_{ff} = 5$ per cent), but with different SN feedback strengths: $E_{SNII} = 10^{51}$ erg (n01e5), 2×10^{51} erg (n01e5SN2), 5×10^{51} erg (n01e5SN5) as well as with zero SNII feedback energy but metal enrichment (n01e5NFBmet). The panels show the results at $z = 0$ (left) and at $z = 3$ (right). The lines and symbols are described in the caption of Fig. 13. SN feedback has little effect on the $\Sigma_{SFR}-\Sigma_g$ relation at $z = 0$ but does affect the high-redshift relation, although only for very large energy injections ($E_{SNII} \geq 2 \times 10^{51}$ erg).

law. At $z = 3$, a slightly greater effect is found, but only for very large energy injections ($E_{SNII} \geq 2 \times 10^{51}$ erg). The extreme case of $E_{SNII} = 5 \times 10^{51}$ erg (n01e5SN5) is comparable to a lowering star formation efficiency to $\epsilon_{ff} = 2$ per cent (n01e2). None of the strong

feedback simulations regulates star formation enough to reproduce the low Σ_{SFR} values found for $\epsilon_{ff} = 1$ per cent (n01e1). This $z \sim 3$ insensitivity of the $K-S$ relation to feedback was also found by Kravtsov (2003).

8 DISCUSSION AND CONCLUSIONS

In this paper we have presented a set of AMR simulations studying the assembly of large Milky Way-like disc galaxies. The self-consistent formation of a late-type disc galaxy has remained elusive in the field of numerical galaxy formation, mainly due to the strong loss of angular momentum in the galaxy assembly process. A popular solution to this problem is to regulate star formation at high redshift via supernova explosions that drive galactic winds, transporting material out of star-forming regions hence lowering the local star formation rate.

We have investigated the plausibility of this mechanism in comparison to a small-scale ($\sim 100\,\mathrm{pc}$) physical approach where star formation is made inefficient by modifying the Schmidt-law star formation normalization. In a very crude way, this mimics unresolved physics such as H_2 formation, small-scale turbulence and radiative effects. We find that the Schmidt-law efficiency of star formation is a far more successful way of regulating star formation towards realistic galaxies than what can be achieved via supernova feedback. Our most successful models reproduce Milky Way galaxies with flat rotation curves, where the small bulge component is formed via secular processes. The main conclusions of this work can be summarized as follows.

(i) Disc characteristics such as $\Sigma_*(r)$, $\Sigma_{\mathrm{gas}}(r)$, $v_{\mathrm{rot}}(r)$ and B/D strongly depend on the choice of star formation efficiency per free-fall time, ϵ_{ff}. The parameter will essentially set the mode of global star formation, hence governing the final spiral Hubble type, where low efficiencies of $\epsilon_{\mathrm{ff}} \sim 1$ per cent render discs of Sb or Sbc type, while $\epsilon_{\mathrm{ff}} = 5$ per cent moves the discs closer to Sa/S0 types. Simulations at low efficiencies agree well with observational constraints on disc characteristics (Courteau 1997; Gnedin et al. 2007), as well as the angular momentum content of disc galaxies (Navarro & Steinmetz 2000), the Tully–Fisher relationship (Pizagno et al. 2007) and the Σ_{SFR}–Σ_{gas} relation (Kennicutt 1998; Bigiel et al. 2008). The origin of the successful Milky Way-like galaxy formation is a well-motivated suppression of star formation at $z \sim 3$, the epoch at which the violent assembly process would form a slowly rotating bulge in case of efficient star formation.

(ii) Supernova feedback does not regulate star formation efficiently at low input energies. Only when the injected energy per supernova event is five times the canonical value, i.e. 5×10^{51} erg, do we find lower and more realistic B/D ratios in the simulations tuned to the standard Kennicutt (1998) star formation law, leading to a flatter rotational velocity profile, hence resembling the galaxies formed without strong feedback but with a low Schmidt-law efficiency. This comes at the cost of a significantly distorted gas disc at $z = 0$, as well as a less bright stellar disc as gas is expelled into the halo, leaving less fuel for star formation at late times. In essence, we find that changes in ϵ_{ff} can play a much greater role in shaping a spiral galaxy than gas redistribution via supernovae-driven winds.

It is plausible that at very high resolution, or when using a drastically different recipe of supernovae feedback, lower values of E_{SNII} may be successful in regulating the SFE. If so, it will still need to mimic the low efficiency on scales of a few 100 pc which, as argued in this work, can be absorbed by the ϵ_{ff}-term.

(iii) If the star formation efficiency parameter is tuned to match the standard $z = 0$ K–S data (Kennicutt 1998), i.e. requiring on the order of $\epsilon_{\mathrm{ff}} \geq 5$ per cent (e.g. Stinson et al. 2006), star formation is likely to be overestimated at high redshift ($z = 3$) where the amplitudes of Σ_{SFR} are an order of magnitude lower (Wolfe & Chen 2006; Gnedin & Kravtsov 2010b). All efficiencies studied in this work ($\epsilon_{\mathrm{ff}} = 1$–5 per cent) are compatible with modern data

of the THINGS survey (Bigiel et al. 2008) but only when $\epsilon_{\mathrm{ff}} \sim 1$ per cent can the constraints from $z = 3$ data be met and late-type, disc-dominated systems form. As the true SFE varies in space and time, being dependent on small-scale physics governing H_2 formation (see e.g. Gnedin et al. 2009), present-day simulations based on single-valued efficiency parameter have little predictive power.

We argue (see also Gnedin et al. 2009) that the results presented in this paper indicate that other processes in the ISM in addition to, or in conjunction with, supernova feedback are important in explaining the evolution of the galaxy population, as well as regulating observed disc sizes. Some form of outflow process must be responsible for enriching the IGM (Oppenheimer & Davé 2006), which together with an inefficient star formation might explain the faint end of the stellar mass function (Somerville & Primack 1999; Kereš et al. 2009). The same argument can be used for the mass–metallicity relationship (Brooks et al. 2007), although Tassis, Kravtsov & Gnedin (2008) demonstrated that it could be reproduced without supernova-driven outflows. Galaxies of masses considered in this work are situated at the knee of the stellar mass function, where the observed and simulated functions (even without feedback; see Kereš et al. 2009) are in closest agreement. This circumstance might explain why even our simulations without feedback resulted in realistic discs. At this galaxy mass, supernova-driven winds cannot escape the deep potential well, and are impeded by the hot halo. On the other hand, AGN feedback, which recently has been introduced into galaxy formation simulations (Di Matteo, Springel & Hernquist 2005), is probably not relevant for the Milky Way since the black hole might not be massive enough for efficient AGN radio-heating. At higher masses, and/or at high redshift, the inclusion of AGN is probably necessary to correctly reproduce the observed abundances and stellar masses. This is the greatest uncertainty of our work, which we leave for a future study.

The way in which galaxies populate dark matter haloes is an important topic; see e.g. Dutton et al. (2010) and references therein for a compilation of recent observational data and theoretical work. Recently, Guo et al. (2010) [see also Moster et al. (2010) and Behroozi, Conroy & Wechsler (2010)] matched dark matter halo mass function from cosmological N-body simulations to the stellar mass function of the galaxies from the SDSS (Li & White 2009). This analysis yields the required galaxy formation efficiency, $\eta = (M_*/M_{\mathrm{halo}})(\Omega_{\mathrm{m}}/\Omega_{\mathrm{b}})$, i.e. what fraction of the universal baryons that must have condensed into stars at a given halo mass. In our 'best-case' model (n01e1ML; see Table 1), the total stellar and dark matter halo virial mass is $\sim 10^{11}\,\mathrm{M}_\odot$ and $\sim 10^{12}\,\mathrm{M}_\odot$, respectively. This results in a stellar fraction of 10 per cent, which corresponds to almost 60 per cent of the cosmic baryon fraction. The rest of the baryons reside in the stellar halo, gaseous disc and ionized gas halo. At this halo mass, abundance matching requires that the stellar disc accounts for only ~ 20 per cent of the cosmic baryon fraction, i.e. a factor of 3 lower. Similar discrepancies exist in all modern work of numerical galaxy formation (Abadi et al. 2003a; Okamoto et al. 2005; Governato et al. 2007; Piontek & Steinmetz 2009b; Scannapieco et al. 2009), and their origin is not yet know, although AGN is a compelling mechanism at the high-mass end, as discussed above. This issue is the topic of a follow-up paper in preparation.

Behroozi et al. (2010) performed a comprehensive analysis of abundance matching, accounting for systematic errors in e.g. the stellar mass estimates, the halo mass function, cosmology etc. Our simulated galaxy formation efficiencies would be in $\sim 2\sigma$ agreement with their result (see their fig. 11). We note that our own Galaxy and

M31 also might be strong outliers in this analysis, considering the inferred η from mass modelling (Klypin, Zhao & Somerville 2002; Seigar, Barth & Bullock 2008) as well as via recent MW halo mass estimates (Xue et al. 2008).

Abundance matching is insensitive to the actual Hubble types of the galaxies, forcing all galaxies of a specific mass to be linked to only one halo mass. At the stellar mass scale of the Milky Way (5–$7 \times 10^{10}\,M_\odot$), only ~ 25 per cent of galaxies are of Sb/Sbc type (Nair & Abraham 2010). It is plausible that the more active merger histories associated with ellipticals and early-type disc galaxies have led to a stronger mass expulsion, via e.g. AGN, in comparison to the more disc-dominated counterparts. In this scenario, late-type discs are expected to be outliers in the galaxy formation efficiency versus stellar mass relation, considering the strong bias towards early-type systems. A detailed subdivision into Hubble types has not yet been performed when matching galaxies to haloes, although colour separations into red and blue systems have been made in studies using weak-lensing (Mandelbaum et al. 2006) and satellite kinematics (More et al. 2010). These studies indicate a different galaxy formation efficiency for galaxies similar in mass to the Milky Way; a late-type galaxy is associated with a halo of ~ 0.5 dex lower halo mass compared to an equally massive early type (see e.g. fig. 11 in More et al. 2010).

Understanding, from a numerical perspective, the spread of baryon fractions across dark matter haloes of different masses, accretion histories and environments is a complicated problem, and will require a large sample of high-resolution simulations, which we leave for a future investigation.

REFERENCES

Abadi M. G., Navarro J. F., Steinmetz M., Eke V. R., 2003a, ApJ, 591, 499
Abadi M. G., Navarro J. F., Steinmetz M., Eke V. R., 2003b, ApJ, 597, 21
Agertz O. et al., 2007, MNRAS, 380, 963
Agertz O., Lake G., Teyssier R., Moore B., Mayer L., Romeo A. B., 2009, MNRAS, 392, 294
Agertz O., Teyssier R., Moore B., 2009, MNRAS, 397, L64
Behroozi P. S., Conroy C., Wechsler R. H., 2010, ApJ, 717, 379
Bigiel F., Leroy A., Walter F., Brinks E., de Blok W. J. G., Madore B., Thornley M. D., 2008, AJ, 136, 2846
Brandt A., 1977, Math. Comp., 31, 333
Bregman J. N., 2007, ARA&A, 45, 221
Brooks A. M., Governato F., Booth C. M., Willman B., Gardner J. P., Wadsley J., Stinson G., Quinn T., 2007, ApJ, 655, L17
Courteau S., 1997, AJ, 114, 2402
Courteau S., de Jong R. S., Broeils A. H., 1996, ApJ, 457, L73
Croft R. A. C., Di Matteo T., Springel V., Hernquist L., 2009, MNRAS, 400, 43
Debattista V. P., Mayer L., Carollo C. M., Moore B., Wadsley J., Quinn T., 2006, ApJ, 645, 209
Dekel A., Silk J., 1986, ApJ, 303, 39
Dekel A. et al., 2009, Nat, 457, 451
Di Matteo T., Springel V., Hernquist L., 2005, Nat, 433, 604
Dijkstra M., Haiman Z., Rees M. J., Weinberg D. H., 2004, ApJ, 601, 666
Dubois Y., Teyssier R., 2008, A&A, 477, 79
Dutton A. A., van den Bosch F. C., 2009, MNRAS, 396, 141
Dutton A. A., Conroy C., van den Bosch F. C., Prada F., More S., 2010, MNRAS, 407, 2
Efstathiou G., 2000, MNRAS, 317, 697
Eskridge P. B. et al., 2002, ApJS, 143, 73
Fall S. M., Efstathiou G., 1980, MNRAS, 193, 189
Garnett D. R., 2002, ApJ, 581, 1019
Gerritsen J. P. E., 1997, PhD thesis, Groningen Univ., the Netherlands
Gingold R. A., Monaghan J. J., 1977, MNRAS, 181, 375
Gnedin N. Y., 2000, ApJ, 535, 530
Gnedin N. Y., Kravtsov A. V., 2010a, preprint (arXiv:1004.0003)
Gnedin N. Y., Kravtsov A. V., 2010b, ApJ, 714, 287
Gnedin O. Y., Weinberg D. H., Pizagno J., Prada F., Rix H., 2007, ApJ, 671, 1115
Gnedin N. Y., Tassis K., Kravtsov A. V., 2009, ApJ, 697, 55
Governato F. et al., 2004, ApJ, 607, 688
Governato F., Willman B., Mayer L., Brooks A., Stinson G., Valenzuela O., Wadsley J., Quinn T., 2007, MNRAS, 374, 1479
Governato F. et al., 2009, MNRAS, 398, 312
Governato F. et al., 2010, Nat, 463, 203
Graham A. W., Worley C. C., 2008, MNRAS, 388, 1708
Guo Q., White S., Li C., Boylan-Kolchin M., 2010, MNRAS, 404, 1111
Haardt F., Madau P., 1996, ApJ, 461, 20
Hoeft M., Yepes G., Gottlöber S., Springel V., 2006, MNRAS, 371, 401
Kalirai J. S., Hansen B. M. S., Kelson D. D., Reitzel D. B., Rich R. M., Richer H. B., 2008, ApJ, 676, 594
Katz N., 1992, ApJ, 391, 502
Kay S. T., Pearce F. R., Frenk C. S., Jenkins A., 2002, MNRAS, 330, 113
Kennicutt R. C., Jr, 1998, ApJ, 498, 541
Kennicutt R. C., Jr et al., 2007, ApJ, 671, 333
Kereš D., Katz N., Weinberg D. H., Davé R., 2005, MNRAS, 363, 2
Kereš D., Katz N., Fardal M., Davé R., Weinberg D. H., 2009, MNRAS, 395, 160
Klypin A., Kravtsov A. V., Valenzuela O., Prada F., 1999, ApJ, 522, 82
Klypin A., Zhao H., Somerville R. S., 2002, ApJ, 573, 597
Komatsu E. et al., 2009, ApJS, 180, 330
Kormendy J., Kennicutt R. C., Jr, 2004, ARA&A, 42, 603
Kravtsov A. V., 2003, ApJ, 590, L1
Kroupa P., Tout C. A., Gilmore G., 1993, MNRAS, 262, 545
Krumholz M. R., Tan J. C., 2007, ApJ, 654, 304
Krumholz M. R., McKee C. F., Tumlinson J., 2009, ApJ, 699, 850
Laurikainen E., Salo H., Buta R., Knapen J. H., Comerón S., 2010, MNRAS, 405, 1089
Leroy A. K., Walter F., Brinks E., Bigiel F., de Blok W. J. G., Madore B., Thornley M. D., 2008, AJ, 136, 2782
Li C., White S. D. M., 2009, MNRAS, 398, 2177
Lucy L. B., 1977, AJ, 82, 1013
McGaugh S. S., Schombert J. M., Bothun G. D., de Blok W. J. G., 2000, ApJ, 533, L99
McGaugh S. S., Schombert J. M., de Blok W. J. G., Zagursky M. J., 2010, ApJ, 708, L14
McKee C. F., Ostriker E. C., 2007, ARA&A, 45, 565
McKee C. F., Ostriker J. P., 1977, ApJ, 218, 148
Mac Low M., Ferrara A., 1999, ApJ, 513, 142
Mac Low M. M., Klessen R. S., 2004, Rev. Modern Phys., 76, 125
Mandelbaum R., Seljak U., Kauffmann G., Hirata C. M., Brinkmann J., 2006, MNRAS, 368, 715
Marcolini A., D'Ercole A., Brighenti F., Recchi S., 2006, MNRAS, 371, 643
Martig M., Bournaud F., 2010, ApJ, 714, L275
Mathewson D. S., Ford V. L., Buchhorn M., 1992, ApJS, 81, 413
Mathieu A., Merrifield M. R., Kuijken K., 2002, MNRAS, 330, 251
Misiriotis A., Xilouris E. M., Papamastorakis J., Boumis P., Goudis C. D., 2006, A&A, 459, 113
Mo H. J., Mao S., White S. D. M., 1998, MNRAS, 295, 319

Moore B., Ghigna S., Governato F., Lake G., Quinn T., Stadel J., Tozzi P., 1999, ApJ, 524, L19

More S., van den Bosch F. C., Cacciato M., Skibba R., Mo H. J., Yang X., 2010, preprint (arXiv:1003.3203)

Mori M., Burkert A., 2000, ApJ, 538, 559

Moster B. P., Somerville R. S., Maulbetsch C., van den Bosch F. C., Macciò A. V., Naab T., Oser L., 2010, ApJ, 710, 903

Murray N., Quataert E., Thompson T. A., 2010, ApJ, 709, 191

Nair P. B., Abraham R. G., 2010, ApJS, 186, 427

Navarro J. F., Benz W., 1991, ApJ, 380, 320

Navarro J. F., Steinmetz M., 2000, ApJ, 538, 477

Navarro J. F., White S. D. M., 1993, MNRAS, 265, 271

Navarro J. F., White S. D. M., 1994, MNRAS, 267, 401

Okamoto T., Eke V. R., Frenk C. S., Jenkins A., 2005, MNRAS, 363, 1299

Oppenheimer B. D., Davé R., 2006, MNRAS, 373, 1265

Oppenheimer B. D., Davé R., Kereš D., Fardal M., Katz N., Kollmeier J. A., Weinberg D. H., 2010, MNRAS, 406, 2325

Pato M., Agertz O., Bertone G., Moore B., Teyssier R., 2010, Phys. Rev. D, 82, 023531

Peebles P. J. E., 1969, ApJ, 155, 393

Pelupessy F. I., Papadopoulos P. P., 2009, ApJ, 707, 954

Piontek F., Steinmetz M., 2009a, preprint (arXiv:0909.4156)

Piontek F., Steinmetz M., 2009b, preprint (arXiv:0909.4167)

Pizagno J. et al., 2007, AJ, 134, 945

Pohlen M., Trujillo I., 2006, A&A, 454, 759

Quinn T., Katz N., Efstathiou G., 1996, MNRAS, 278, L49

Rafelski M., Wolfe A. M., Cooke J., Chen H., Armandroff T. E., Wirth G. D., 2009, ApJ, 703, 2033

Raiteri C. M., Villata M., Navarro J. F., 1996, A&A, 315, 105

Rasera Y., Teyssier R., 2006, A&A, 445, 1

Read J. I., Hayfield T., Agertz O., 2010, MNRAS, 405, 1513

Robertson B. E., Kravtsov A. V., 2008, ApJ, 680, 1083

Robertson B., Yoshida N., Springel V., Hernquist L., 2004, ApJ, 606, 32

Romeo A. B., 1994, A&A, 286, 799

Romeo A. B., Agertz O., Moore B., Stadel J., 2008, ApJ, 686, 1

Rosen A., Bregman J. N., 1995, ApJ, 440, 634

Roškar R., Debattista V. P., Stinson G. S., Quinn T. R., Kaufmann T., Wadsley J., 2008, ApJ, 675, L65

Sawala T., Scannapieco C., Maio U., White S., 2010, MNRAS, 402, 1599

Scannapieco C., Tissera P. B., White S. D. M., Springel V., 2006, MNRAS, 371, 1125

Scannapieco C., White S. D. M., Springel V., Tissera P. B., 2009, MNRAS, 396, 696

Schmidt M., 1959, ApJ, 129, 243

Schuster K. F., Kramer C., Hitschfeld M., Garcia-Burillo S., Mookerjea B., 2007, A&A, 461, 143

Seigar M. S., Barth A. J., Bullock J. S., 2008, MNRAS, 389, 1911

Shen J., Sellwood J. A., 2006, MNRAS, 370, 2

Somerville R. S., Primack J. R., 1999, MNRAS, 310, 1087

Sommer-Larsen J., Götz M., Portinari L., 2003, ApJ, 596, 47

Springel V., Hernquist L., 2003, MNRAS, 339, 289

Stinson G., Seth A., Katz N., Wadsley J., Governato F., Quinn T., 2006, MNRAS, 373, 1074

Stinson G. S., Dalcanton J. J., Quinn T., Gogarten S. M., Kaufmann T., Wadsley J., 2009, MNRAS, 395, 1455

Sutherland R. S., Dopita M. A., 1993, ApJS, 88, 253

Tasker E. J., Tan J. C., 2009, ApJ, 700, 358

Tassis K., Kravtsov A. V., Gnedin N. Y., 2008, ApJ, 672, 888

Teyssier R., 2002, A&A, 385, 337

Thielemann F., Nomoto K., Yokoi K., 1986, A&A, 158, 17

Thoul A. A., Weinberg D. H., 1996, ApJ, 465, 608

Tully R. B., Fisher J. R., 1977, A&A, 54, 661

Valcke S., de Rijcke S., Dejonghe H., 2008, MNRAS, 389, 1111

van den Bergh S., McClure R. D., 1994, ApJ, 425, 205

Wada K., Norman C. A., 2007, ApJ, 660, 276

Weinzirl T., Jogee S., Khochfar S., Burkert A., Kormendy J., 2009, ApJ, 696, 411

White S. D. M., Rees M. J., 1978, MNRAS, 183, 341

Wolfe A. M., Chen H., 2006, ApJ, 652, 981

Wong T., Blitz L., 2002, ApJ, 569, 157

Xue X. X. et al., 2008, ApJ, 684, 1143

Zhang W., Li C., Kauffmann G., Zou H., Catinella B., Shen S., Guo Q., Chang R., 2009, MNRAS, 397, 1243

APPENDIX A: EFFECT OF RESOLUTION

The numerical set-up in the SR5-n1e1ML simulation is identical to SR6-n1e1ML, apart from having twice as high spatial resolution and hence eight times the mass resolution (see Table 1). In Fig. A1 we plot the resulting stellar surface densities and circular velocities from the simulations. We find very little difference apart from more gas being consumed in SR5-n1e1ML resulting in a more massive disc (by ∼35 per cent) at higher resolution and the bulge mass is lowered by ∼20 per cent. The dark halo is less contracted but as $M(<r)$ remains roughly the same, the circular velocities change little.

Why do we not see any striking differences in the higher-resolution simulation? At the adopted resolutions we do not uncover more physics with only a factor of 2 increase in spatial resolution:
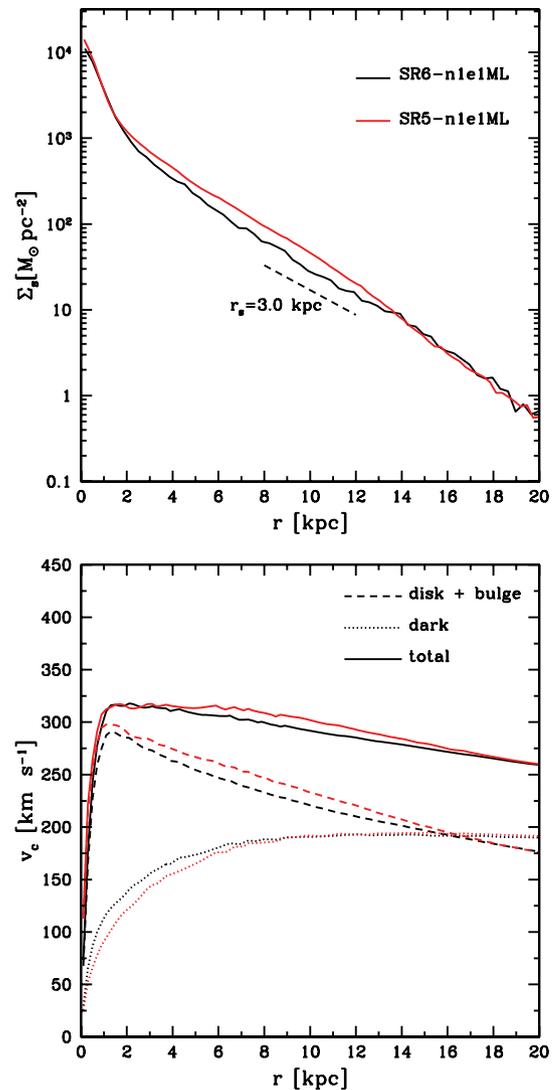

Figure A1. Stellar surface densities (top) and circular velocities (bottom) in SR6-n1e1ML (black line) and SR5-n1e1ML (red line).

we are still under-resolving the scaleheight and are not resolving individual star-forming clouds. At much higher resolution this conclusion will change and the numerical parameters will have a different meaning.

APPENDIX B: RESOLVING STAR FORMATION

In this appendix we derive a simple relationship of the required resolution (Δx) and star formation density threshold (n_0) required to capture star formation in an extended disc at the current epoch. Let us assume that a gas disc at $z = 0$ follows an exponential radial density profile with a sech^2 vertical profile, i.e.

$$\rho(r, z) = \rho_0 \, \text{sech}^2(-z/h) \exp(-r/r_d). \tag{B1}$$

The mass of this profile can be integrated from equation (B1) to give us the characteristic-scale disc density

$$\rho_0 = M_d / 4\pi h \, r_d^2. \tag{B2}$$

Assume that this density distribution is coarsened on a regular mesh with a cell size Δx, and that the disc is aligned to a mesh axis. The physical density in a central strip of cells can then be calculated as

$$\rho(r)_{\Delta x} = \frac{M_d}{4\pi h \, r_d^2 \Delta x} \exp(-r/r_d) \left(\int_{-\Delta x/2.0}^{\Delta x/2.0} \text{sech}^2(-z/h) \, \text{d}z \right) \tag{B3}$$

$$= \frac{M_d}{4\pi h \, r_d^2 \Delta x} \exp(-r/r_d) h \, [-\tanh(-z/h)]_{-\Delta x/2.0}^{\Delta x/2.0} . \tag{B4}$$

The true star-forming scaleheight of cold molecular gas is on the order of $\sim 10\,\text{pc}$, and for the neutral atomic ISM it is $\sim 100\,\text{pc}$. Galaxy formation simulations under-resolve this structure, and it is safe to assume that the effective numerical scaleheight $h \sim \Delta x$, until Δx goes below a few tens of parsecs. Under this assumption the integration limits in the sech^2 term above will always be from $-z/h = -0.5$ to $z/h = 0.5$. Equation (5) can now be simplified to

$$\rho(r)_{\Delta x} = 0.924 \frac{M_d}{4\pi h \, r_d^2 \Delta x} \exp(-r/r_d), \tag{B5}$$

which in units of particles per cm^{-3} is approximately

$$n(r)_{\Delta x} \approx \left(\frac{M_d}{10^9 \, \text{M}_\odot} \right) \frac{3 \exp(-r/r_d)}{\Delta x \, r_d^2} \quad \text{cm}^{-3}. \tag{B6}$$

We can rearrange this equation and write down the following useful relationship:

$$r = r_d \ln \left[\left(\frac{M_d}{10^9 \, \text{M}_\odot} \right) \frac{3}{\Delta x \, r_d^2 n_{\Delta x}} \right]. \tag{B7}$$

This equation tells us at which radius, given a cell size, we cross the density $n_{\Delta x}$. In Section 5.1 we argued that using $n = 1\,\text{cm}^{-3}$ and $\Delta x = 340\,\text{pc}$ resulted in less realistic galaxies as star formation was 'missing' at large radii. Inserting these values into equation (B7) gives us $r \sim 6$–$8\,\text{kpc}$ for any reasonable choice of r_d, confirming the arguments of Section 5.1. Adopting $n = 0.1\,\text{cm}^{-3}$ increases the star-forming radius by a factor of 2.3.

This paper has been typeset from a TEX/LATEX file prepared by the author.